

PAPER • OPEN ACCESS

Role of the separatrix density in the pedestal performance in deuterium low triangularity JET-ILW plasmas and comparison with JET-C

To cite this article: L. Frassinetti *et al* 2021 *Nucl. Fusion* **61** 126054

View the [article online](#) for updates and enhancements.

You may also like

- [Plasma performance and operational space without ELMs in DIII-D](#)
C Paz-Soldan and the DIII-D Team
- [Dynamics and stability of divertor detachment in H-mode plasmas on JET](#)
A R Field, I Balboa, P Drewelow et al.
- [Numerical analyses of JT-60SA tokamak with tungsten divertor by COREDIV code](#)
K Gazka, I Ivanova-Stanik, W Stpniewski et al.

Role of the separatrix density in the pedestal performance in deuterium low triangularity JET-ILW plasmas and comparison with JET-C

L. Frassinetti^{1,*}, C. Perez von Thun², B. Chapman³, A. Fil³, J.C. Hillesheim³, L. Horvath³, G.T.A. Huijsmans⁴, H. Nyström¹, V. Parail³, S. Saarelma³, G. Szepesi³, B. Viola³, R. Bianchetti Morales³, M. Dunne⁵, A.R. Field³, J. Flanagan³, J.M. Fontdecaba⁶, D. Hatch⁷, B. Lomanowski⁸, C.F. Maggi³, S. Menmuir³, S. Pamela³, C.M. Roach³, E. Rachlew¹, E.R. Solano⁶ and JET Contributors^{9,a}

¹ Division of Fusion Plasma Physics, KTH, Stockholm, Sweden

² Institute of Plasma Physics and Laser Microfusion (IPPLM), Hery 23, 01-497 Warsaw, Poland

³ CCFE, Culham Science Centre, Abingdon, OX14 3DB, United Kingdom of Great Britain and Northern Ireland

⁴ CEA, IRFM, 13108 Saint-Paul-Lez-Durance, France

⁵ Max-Planck-Institut für Plasmaphysik, Garching, Germany

⁶ Laboratorio Nacional de Fusión, CIEMAT, Madrid, Spain

⁷ Institute for Fusion Studies, University of Texas at Austin, Austin, United States of America

⁸ Oak Ridge National Laboratory, Oak Ridge, TN 37831, United States of America

⁹ EUROfusion Consortium, JET, Culham Science Centre, Abingdon, OX14 3DB, United Kingdom of Great Britain and Northern Ireland

E-mail: lorenzof@kth.se

Received 1 June 2021, revised 13 September 2021

Accepted for publication 26 October 2021

Published 22 November 2021



Abstract

A reduction of the pedestal pressure with increasing separatrix density over pedestal density ($n_e^{\text{sep}}/n_e^{\text{ped}}$) has been observed in JET. The physics behind this correlation is investigated. The correlation is due to two distinct mechanisms. The increase of $n_e^{\text{sep}}/n_e^{\text{ped}}$ till ≈ 0.4 shifts the pedestal pressure radially outwards, decreasing the peeling-balloning stability and reducing the pressure height. The effect of the position saturates above $n_e^{\text{sep}}/n_e^{\text{ped}} \approx 0.4$. For higher values, the reduction of the pedestal pressure is ascribed to increased turbulent transport and, likely, to resistive MHD effects. The increase of $n_e^{\text{sep}}/n_e^{\text{ped}}$ above ≈ 0.4 reduces $\nabla n_e/n_e$, increasing η_e and the pedestal turbulent transport. This reduces the pressure gradient and the pedestal temperature, producing an increase in the pedestal resistivity. The work suggests that the increase in resistivity might destabilize resistive balloning modes, further reducing the pedestal stability.

* Author to whom any correspondence should be addressed.

^a See Joffrin *et al* 2019 (<https://doi.org/10.1088/1741-4326/ab2276>) for the JET Contributors.



Original content from this work may be used under the terms of the [Creative Commons Attribution 4.0 licence](https://creativecommons.org/licenses/by/4.0/). Any further distribution of this work must maintain attribution to the author(s) and the title of the work, journal citation and DOI.

Keywords: pedestal, JET, peeling-ballooning stability, EPED, Europed, separatrix density

(Some figures may appear in colour only in the online journal)

1. Introduction

Understanding the physics of the pedestal in metal wall machines is vital to reach reliable predictions for future experiments and to optimize their performances. In 2011, JET changed the wall material from carbon (JET-C) to tungsten in the divertor and beryllium in the main chamber (JET-ILW) [1, 2]. The initial JET-C/JET-ILW pedestal comparisons [3] showed a similar pedestal performance in hybrid plasmas while the pedestal pressure was $\approx 20\%$ lower with the metal wall in baseline plasmas. In recent years, JET-ILW has recovered good confinement also in baseline plasmas [4, 5], but the full understanding of the initial JET-ILW pedestal degradation remains unclear. In the past years, several experimental results have identified specific parameters that might be linked to the pedestal degradation. One of these parameters is the intrinsic low-Z impurities [6]. JET-ILW has no intrinsic carbon impurities and low-Z impurity seeding (such as nitrogen, carbon or neon) has led to an increased pedestal pressure [6–8]. Similar results have been obtained in other machines [9–13]. Another important parameter is the main gas rate, which tends to be relatively high in JET-ILW due to operational constraints [14, 15]. For example, a comparison of the pressure profiles in AUG with C wall and with W wall has shown that, without gas puffing, the pedestal pressure does not depend on the wall material [16]. Strongly correlated to gas rate and recycling, the position of the electron pedestal density (n_e^{pos}) is another important parameter [17–19], as also noted in AUG [20] and DIII-D [21]. Here n_e^{pos} is defined as the position of the maximum gradient in the pedestal region. The increasing gas rate can lead to the n_e outward radial shift, destabilizing the peeling-ballooning (PB) modes and reducing the pedestal stability. Changes in n_e^{pos} can be due also to different recycling and different divertor geometry, as noted for example in DIII-D [21–23]. Unfortunately, the effect of n_e^{pos} on the ideal PB stability does not seem to explain the pedestal degradation at high gas rate [17, 24].

In recent years, experimental studies have shown that the electron separatrix density (n_e^{sep}) might play a significant role in pedestal physics as well. Experimental results achieved in AUG [20], Alcator C-Mod [13] and JET-ILW [24] have identified empirical correlations between the electron pedestal pressure (p_e^{ped}) and n_e^{sep} . An explanation of this correlation has been identified only at low separatrix density where the pedestal degradation has been ascribed to the destabilizing effect of the outward radial shift of the density [20, 24].

To complicate the understanding of the pedestal behaviour, the ideal PB stability does not seem to explain the ELM triggering mechanism in all type I ELMy H-modes. For example, it has been shown that in some DIII-D plasmas the pedestal

gradients can saturate before the ELM is triggered, with the pedestal remaining in a metastable state [25, 26], as observed also in JET-ILW [27]. In JET-ILW, several results have shown that, in a large part of type I ELMy H-modes, the ELM is triggered before the ideal PB boundary is reached [3, 15, 18, 24, 27, 28]. From the point of view of engineering parameters, this problem occurs at high deuterium gas rate (Γ_{D2}) and high power, see [15]. However, universal thresholds in power and gas rate valid for all JET-ILW plasmas could not be found [24]. To describe the problem related to the ideal PB stability, a more appropriate parameter could be the relative shift (the distance between the pedestal position of electron density and temperature, $n_e^{\text{pos}} - T_e^{\text{pos}}$). In fact, a clear positive correlation between the distance of the experimental pedestal from the ideal PB stability boundary and $n_e^{\text{pos}} - T_e^{\text{pos}}$ has been observed for a wide dataset [24]. The two results are consistent among each other, because pedestals with high Γ_{D2} and high P_{sep} are found to have high relative shift. ($n_e^{\text{pos}} - T_e^{\text{pos}}$ increases both with increasing gas rate and with increasing power [24]). So far, no explanation for the correlation between the disagreement with ideal MHD and the relative shift has been found. Moreover, the mechanism that triggers the ELMs in ideally PB stable JET-ILW pedestals is still elusive. Based on the results discussed in this work, section 9 and section 10.2 will propose a possible mechanism.

The present work investigates the links between the increasing gas rate, the separatrix density and the pedestal degradation in deuterium low triangularity JET plasma. The work identifies a clear empirical link between p_e^{ped} and the ratio $n_e^{\text{sep}}/n_e^{\text{ped}}$. Then, the work investigates the underlying physics behind this correlation showing that two physics mechanisms are active, one acting at low $n_e^{\text{sep}}/n_e^{\text{ped}}$ and one acting at high $n_e^{\text{sep}}/n_e^{\text{ped}}$. Finally, the work proposes a possible mechanism to explain the problem related to the ideal PB stability and its link to the high relative shift. The results suggest that the different $n_e^{\text{sep}}/n_e^{\text{ped}}$ typical of JET-C and JET-ILW plasmas might be one of the reason for the different pedestal performance with the two walls. Other mechanisms, such as the role of low-Z impurities, are not discussed.

The paper is organized as follows. Section 2 describes the datasets used in the work. Section 3 describes the data analysis technique and the main modelling tools. Section 4 presents the empirical correlations between pedestal pressure and separatrix density in JET. Section 5 describes the qualitative modelling performed to understand the link between gas rate, $n_e^{\text{sep}}/n_e^{\text{ped}}$ and n_e^{pos} . Section 6 describes the role of n_e^{pos} in explaining the negative correlation between pedestal pressure and $n_e^{\text{sep}}/n_e^{\text{ped}}$. Section 7 discusses the turbulent transport and its correlation with $n_e^{\text{sep}}/n_e^{\text{ped}}$. Section 8 presents empirical links between the turbulent transport with the pedestal width

and with the problem related to ideal MHD stability. Section 9 presents the first results on the possible role of resistivity in determining the PB stability. Finally, section 10 presents discussion and conclusions.

2. Datasets used

The work is based on a dataset composed of three subsets of low- δ JET-ILW deuterium plasmas performed at 2 MA and 2.3 T with different deuterium gas rate (Γ_{D2}). Each of the three subsets is characterized by constant β_N (respectively $\beta_N = 1.2$, $\beta_N = 1.5$ and $\beta_N = 1.9$) obtained by operating the NBI in feedback. The gas rate is in the range $\Gamma_{D2} = 0.4 \times 10^{22} - 6.0 \times 10^{22} \text{ e s}^{-1}$ and the NBI power in the range $P_{NBI} = 8 - 24 \text{ MW}$. For each value of gas rate and β_N , the dataset has both plasmas with the outer strike point (o.s.p.) on the horizontal target (far from the cryo-pump) and in the corner (close to the cryo-pump). The geometry for the two configurations can be found, for example, in reference [24]. The two divertor configurations are used to change n_e^{sep} also via a different pumping efficiency (and recycling) and not only via the gas rate. The β_N vs Γ_{D2} diagram of the three constant β_N datasets is shown in figure 1(a). The use of constant β_N is important to remove the β_N effect on the pedestal stability and allow the study of the direct effect of n_e^{sep} on the pedestal performance.

For comparison, a set of JET-C deuterium plasmas at 2 MA, 2.3 T and low triangularity is also used. The JET-C dataset consists of eight shots at $\beta_N = 1.5$ and one shot at $\beta_N = 1.9$. The NBI power is in the range $P_{NBI} = 6 - 8 \text{ MW}$ at $\beta_N = 1.5$ and $P_{NBI} = 20 \text{ MW}$ at $\beta_N = 1.9$. The gas rate is in the range $\Gamma_{D2} = 0.0 - 0.4 \times 10^{22} \text{ e s}^{-1}$, significantly lower than the gas rate of the JET-ILW dataset. This is because JET-C was used to operate with no or very low Γ_{D2} , while for operational constraints (to mitigate W influx) JET-ILW tends to operate with higher gas rate [14]. At low- δ , no JET-C/JET-ILW pair of pulses can be found with identical engineering parameters (including Γ_{D2}).

The above described datasets are the main one used in this work and hereafter they are named as the ‘constant β_N datasets’. These datasets are represented throughout the work using coloured circles (JET-ILW) and coloured triangles (JET-C). The colours have been used to highlight the value of β_N . Full symbols are used for the corner configuration and empty symbols for the horizontal configuration. The colour/symbol definitions are shown in figure 1(a) and are used consistently throughout the work.

These datasets can be recast into subsets of power scans with similar gas rate but different β_N . These subsets have been used only to verify the ELM type. Figure 1(b) shows the correlation between the ELM frequency (f_{ELM}) and the power through the separatrix (P_{sep}), with the colours that highlight subsets with similar gas rate. The positive correlation between f_{ELM} and P_{sep} shows that the pulses are characterized by type I ELMs [29].

Finally, the key experimental results are strengthened by including a wider dataset extracted from the EUROfusion JET-ILW pedestal database [24]. When discussing dimensionless parameters, all the low- δ deuterium unseeded plasmas with

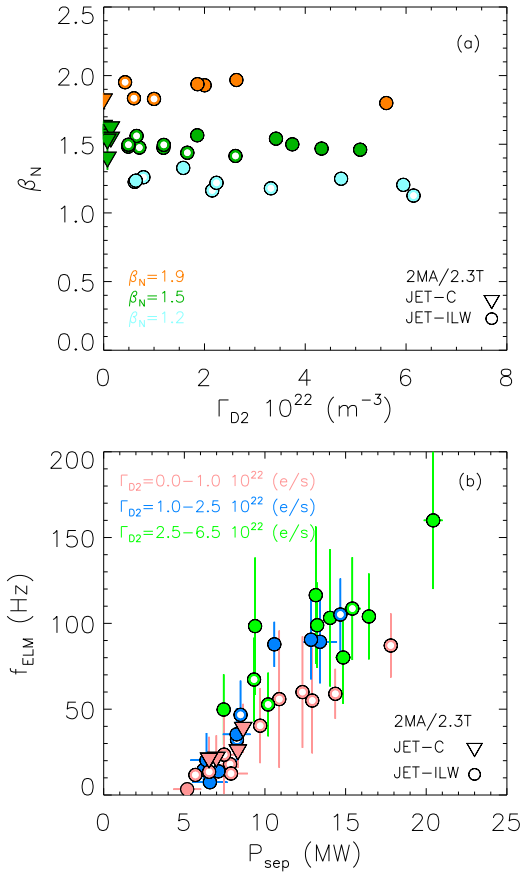


Figure 1. Frame (a) shows the β_N and the gas rate for the three main dataset used in this work. The colours highlight the value of β_N . The circles and the triangles highlight the JET-ILW and JET-C pulses respectively. The full symbols show the plasmas with o.s.p. in the corner and the open symbols those on the horizontal target. Frame (b) shows the correlation between ELM frequency and power through the separatrix for the same dataset of frame (a), but with the colours that highlight subsets similar gas rate. The colour/symbol definitions of frame (a) are used throughout the paper.

no pellets and no RMPs are used. When discussing dimensional parameters, the dataset is further restricted to have $I_p = 1.9 - 2.4 \text{ MA}$, $B_t = 2.1 - 2.4 \text{ T}$, in order to have a range of I_p and B_t roughly consistent with the constant β_N datasets. These extended datasets are represented with grey squares throughout the paper and hereafter they are named as the ‘extended low- δ dataset’.

The modelling results are compared with two JET-ILW reference pulses at $\beta_N = 1.5$ and with the o.s.p. on the horizontal target: the low gas rate pulse #96202 ($\Gamma_{D2} = 0.6 \times 10^{22} \text{ e s}^{-1}$, $P_{\text{abs}} = 14 \text{ MW}$, $n_e^{\text{sep}}/n_e^{\text{ped}} \approx 0.4$) and the high gas pulse #96201 (high gas $\Gamma_{D2} = 2.7 \times 10^{22} \text{ e s}^{-1}$, $P_{\text{abs}} = 18 \text{ MW}$, $n_e^{\text{sep}}/n_e^{\text{ped}} \approx 0.8$). Pedestal profiles and PB stability boundaries for the two reference pulses are discussed in section 3 in figures 2, 4 and 5.

3. Data analysis technique and modelling tools

The first part of the section describes the main diagnostic used for determining the pedestal profiles and the pedestal

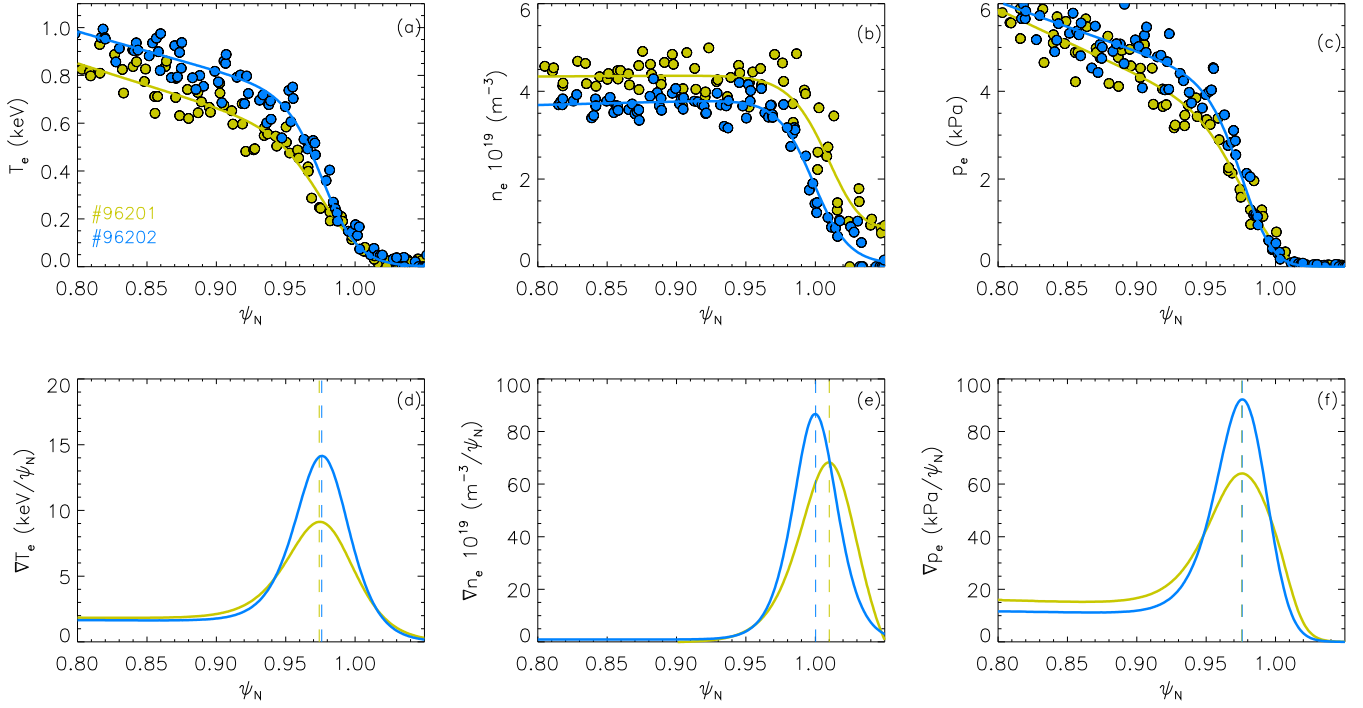


Figure 2. Pre-ELM profiles in the pedestal region of electron temperature (a), density (b) and pressure (c) for the two reference pulses, #96201 (high gas rate) and #96202 (low gas rate) both with $\beta_N = 1.5$ and horizontal configuration. Frames (d)–(f) show the corresponding gradients of temperature, density and pressure. The vertical dashed lines highlight the pedestal positions.

parameters, the data analysis technique and the definitions of the main quantities. The second part describes the modelling tools, with particular emphasis on the PB stability analysis of the pedestal, which is used throughout the paper, and with brief descriptions of the other modelling tools (more specific details are presented in the respective sections).

3.1. Diagnostics and data analysis technique

The pedestal profiles of electron temperature (T_e) and density (n_e) are measured with the Thomson scattering diagnostic [30]. To study the pedestal structure, only the pre-ELM profiles have been considered. These have been defined as the profiles located in the 70%–99% of the ELM cycle. The pre-ELM profiles are then fitted with modified hyperbolic tangent function (mtanh) [31] which in JET describes well the experimental pedestal structure inside the separatrix [32]. Due to possible uncertainties in the absolute position of the experimental data, the profiles are radially shifted to have a separatrix temperature (T_e^{sep}) at 100 eV. The value $T_e^{\text{sep}} = 100$ eV has been determined with the two point model [33]. An application of the model to JET-ILW plasmas with P_{sep} in the range 5–20 MW (comparable to the present ‘constant β_N datasets’ P_{sep}) shows that the separatrix temperature can vary in the range 80 eV–120 eV. Moreover, EDGE2D-EIRENE simulations done in JET-ILW plasmas with power and n_e^{sep} comparable to the present datasets (albeit with slightly different I_p and B_t) shows that T_e^{sep} can vary in the range 90–110 eV in typical gas and power scans. As later discussed, a 10%–20% uncertainty in T_e^{sep} does not affect the conclusion of the present work.

The pedestal height and pedestal width are determined from the mtanh fits to the pre-ELM profiles. The width is expressed in normalized poloidal flux units (ψ_N). The pedestal position is defined as the position of maximum gradient of the mtanh fits and is expressed in ψ_N units. The pedestal gradient is defined as the maximum gradient of the fits. The separatrix density has been determined with two approaches, as (i) the value of the density fit at $\psi_N = 1$ and as (ii) the average of the experimental data in a range $0.01\psi_N$ wide around $\psi_N = 1$ (in both cases, after the 100 eV shift has been applied). The two approaches lead to similar results and in the rest of the work n_e^{sep} from the density fit is used. The uncertainty on n_e^{sep} is determined from the uncertainty in the fit. The pre-ELM profiles and the corresponding gradients for the two reference pulses are shown in figure 2. The high gas rate pulse (#96201) is characterized by lower pedestal temperature and higher density (both at the pedestal top and at the separatrix), than the low gas rate pulse (#96202), see figures 2(a) and (b) respectively. The pedestal pressure and the pedestal pressure gradient are lower in the high gas pulse, see figures 2(c) and (f). The position of the pedestal temperature is similar in the two pulses, see figure 2(d), while the density is more outward in the high gas pulse, figure 2(e). Note that the position of the pedestal pressure (p_e^{pos}) shown in figure 2(f) is similar in the two reference shots, while n_e^{pos} is further out in the high gas pulse. This observation and its implication for the PB stability is discussed in detail in section 6.

Special care is necessary for the definition of the width of the pedestal pressure (w_{p_e}). In the EPED1 model, the width is usually defined as the average between the density and the temperature width, $w_{p_e}^{\text{EPED1}} = (w_{n_e}^{\text{EPED1}} + w_{T_e}^{\text{EPED1}})/2$, with $w_{n_e}^{\text{EPED1}}$

and $w_{T_e}^{\text{EPED1}}$ determined by considering only the part of the pedestal located inside the separatrix. This definition is very reasonable in DIII-D and in the plasmas with low collisionality and low gas rate, where n_e^{pos} is not significantly different from T_e^{pos} . However, in JET-ILW the pedestal density tends to be significantly more radially outwards than the temperature (see for example figure 2 and references [17–19, 24]), with large part of the density outside the separatrix. In these conditions, a large part of steep density gradient is at $\psi_N > 1.0$, so $w_{n_e}^{\text{EPED1}}$ is almost negligible and hence $w_{p_e}^{\text{EPED1}} = (w_{n_e}^{\text{EPED1}} + w_{T_e}^{\text{EPED1}})/2 \approx w_{T_e}^{\text{EPED1}}/2$. Instead, experimentally, these conditions leads to $w_{p_e} \approx w_{T_e}$. So EPED1 definition can lead to a significant underestimation of the experimental w_{p_e} in JET-ILW. A systematic comparison of possible w_{p_e} definitions in JET-ILW can be found in reference [24]. In this work, in order to have a definition that reflects more accurately the experimental pressure, w_{p_e} is defined as the width of the fitted experimental pressure profile. As discussed in section 8, the use of a different definition does not change the qualitative conclusion of the work.

Due to the central role of n_e^{sep} and of the pedestal position in this work, it is necessary to assess how much the uncertainty in T_e^{sep} can affect the conclusions. As can be seen from the sensitivity test of figure 3, a reasonable variations of T_e^{sep} has a small effect on n_e^{sep} and on the pedestal position. The orange profiles in figure 3 shows the n_e and T_e fits shifted to $T_e^{\text{sep}} = 100$ eV for the reference pulse #96202. The other two profiles have a $\pm 20\%$ variation in T_e^{sep} . According to the two-point model and the EDGE2D-EIRENE simulations of reference [34], a larger uncertainty is unlikely in typical JET-ILW power and gas scans. In particular, according to the two point model, T_e^{sep} significantly lower than 100 eV can be reached in JET-ILW only with extremely low P_{sep} . For example, $T_e^{\text{sep}} \approx 50$ eV would be obtained with $P_{\text{sep}} \approx 2$ MW, a value unrealistically low value for the present dataset. Assuming a 20% variation in T_e^{sep} , the change in the pedestal position of the temperature would be in the range $T_e^{\text{pos}} \approx 0.976\text{--}0.981\psi_N$ which is slightly lower than typical error bars ($\approx 0.003\psi_N$) and the change in the separatrix density would be in the range $n_e^{\text{sep}} \approx (1.64\text{--}2.03) \times 10^{19} \text{ m}^{-3}$ which is comparable to the typical n_e^{sep} error bars (whose relative uncertainty is in the range $\approx 5\%\text{--}10\%$). Another example will be discussed in figure 19(a). Moreover, in the present work $n_e^{\text{sep}}/n_e^{\text{ped}}$ varies up to a factor 4, much larger than the possible systematic effect introduced by the T_e^{sep} uncertainty. Earlier sensitivity tests with other datasets have reached similar conclusions [18, 24]. A further discussion on sensitivity of the assumption $T_e^{\text{sep}} \approx 100$ eV is presented in the appendix, where it is shown that even a very large variation of T_e^{sep} , in the range 20–300 eV, would not affect the conclusion of the present work.

The ion temperature is determined with the charge exchange (CX) diagnostics using the pre-ELM T_i profiles. In the dataset used in this work, the CX diagnostics cover the region from the core to the pedestal top but no measurements of T_i^{sep} are available. Figure 4 shows the T_i and the T_e pre-ELM profiles for the two reference pulses, #96201 that has relatively high pedestal collisionality, figure 4(a), #96202

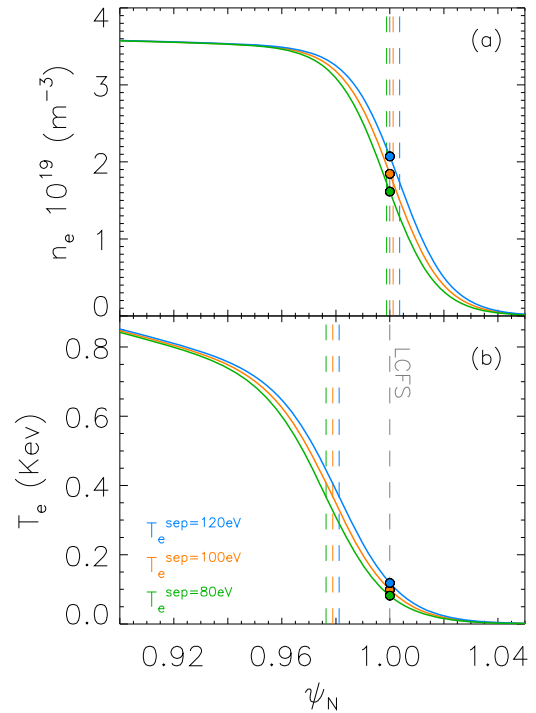


Figure 3. Fit to experimental n_e (a) and T_e (b) pre-ELM profiles for the JET-ILW pulse #96202. The colours highlight three different assumptions for the separatrix temperature. The variation of T_e^{sep} is consistent with the possible variation in power and gas scans modelled with EDGE2D-EIRENE [34]. The dots highlight the corresponding n_e^{sep} and T_e^{sep} . The vertical dashed lines highlight the position of the pedestal and the LCFS.

with relatively low pedestal collisionality, figure 4(b). In both pulses, $T_i = T_e$ holds in the region covered by the CX diagnostics. At the separatrix, based on earlier measurements, it is reasonable to assume $T_i^{\text{sep}} > T_e^{\text{sep}}$. Section 3.2 will discuss that this uncertainty does not affect significantly the conclusions.

The total pressure is determined as $p = p_e + p_i$ using $T_i = T_e$ and with the ion density determined from the electron density and Z_{eff} , with beryllium as main impurity in JET-ILW and carbon in JET-C, using the expression $n_i = n_e(Z_{\text{main}} + 1 - Z_{\text{eff}})/Z_{\text{main}}$. The radial profile of the effective charge Z_{eff} is not available systematically so a line-integrated spectroscopic value has been used for Z_{eff} .

3.2. Modelling tools

3.2.1. Ideal peeling-ballooning stability. The pedestal PB stability is the central modelling part of the work. The stability is determined using the standard JET approach implemented in the HELENA-ELITE workflow [35]. The fixed boundary equilibrium code HELENA is used to determine the equilibrium [36]. The Sauter formula [37] has been used to calculate the bootstrap current (j_{bs}). Then, the linear ideal MHD stability code ELITE [38] is used to determine the PB stability in the j – α space. Here j is the current density, composed of the fully diffused ohmic current and the j_{bs} , and α is the normalized pressure gradient defined as in [39]:

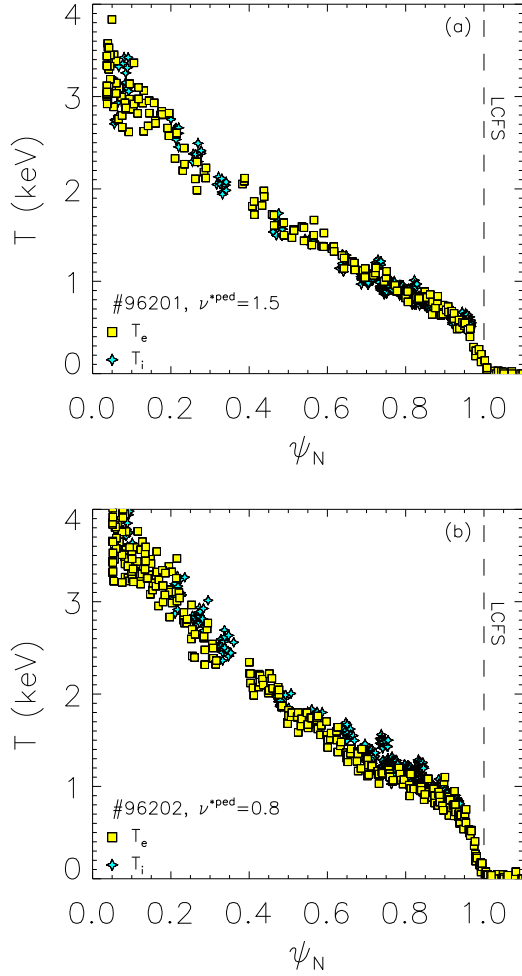


Figure 4. Pre-ELM profiles of electron temperature and ion temperature for the reference pulses used in this work. Frame (a) shows the profiles for pulse #96201 (high gas rate, high $n_e^{\text{sep}}/n_e^{\text{ped}}$ and high collisionality). Frame (b) shows the profiles for pulse #96202 (low gas rate, low $n_e^{\text{sep}}/n_e^{\text{ped}}$ and low collisionality).

$$\alpha = -\frac{2\partial_\psi V}{(2\pi)^2} \left(\frac{V}{2\pi^2 R} \right)^{1/2} \mu_0 p', \quad (1)$$

where V is the plasma volume enclosed by the flux surface, R the major radius and p' the total pressure derivative in the poloidal flux ψ . The stability criterion has been defined as $\gamma < 0.03\omega_A$ (where γ is the growth rate and ω_A is the Alfvén frequency), as usually done for JET-C and JET-ILW pedestal stability analysis [3, 35, 40]. The choice of the stability criterion does not affect significantly the final conclusions, see for example [15]. The MHD stability of the modes from $n = 5$ up to $n = 70$ has been considered. No major difference in the result is expected if higher n modes are included [15].

An example of the PB stability diagram for the reference pulses #96201 and #96202 is shown in figure 5. The full stars highlight the normalized pressure gradients and the peak edge current densities corresponding to the experimental pre-ELM profiles, α_{exp} and j_{exp} respectively. The continuous lines highlight the ideal PB stability boundary. In both pulses, the ELM is triggered before the ideal PB stability boundary is reached. However #96202 is significantly closer to the

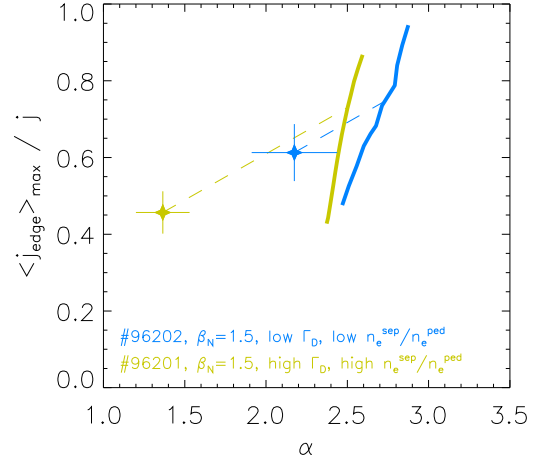


Figure 5. Ideal PB stability for pulses #96201 and #96202. The continuous lines show the PB stability boundary. The full symbols show α and j of the experimental pre-ELM pedestals, while the dashed line highlight the self-consistent path to determine the critical α and j .

boundary than #96201. To quantify this difference, the self-consistent approach described in [35] is used. Starting from the experimental point, the electron temperature is increased, then the current density profile, the equilibrium and the stability are recalculated self-consistently. The dashed lines in figure 5 shows the self-consistent path. The process is repeated till a marginally PB stable pressure profile is obtained. This determines the critical pressure p_e^{crit} , the critical current density j_{crit} and the critical normalized pressure gradient α_{crit} for the comparison with the experimental values. A value $\alpha_{\text{crit}}/\alpha_{\text{exp}} = 1$ implies that the ELMs are triggered when the ideal PB boundary is reached. $\alpha_{\text{crit}}/\alpha_{\text{exp}} \approx 1.85$ for #96201 and $\alpha_{\text{crit}}/\alpha_{\text{exp}} \approx 1.25$ for #96202.

Rotation and diamagnetic effects have not been considered in the PB stability. These terms might affect the stability boundary by 20%–30% [8, 41, 42]. Neglecting the rotation and the diamagnetic term should not modify drastically the conclusions since in the present dataset $\alpha_{\text{crit}}/\alpha_{\text{exp}}$ varies more than a factor two (see section 6).

In determining the PB stability, $T_i = T_e$ has been used, as experimentally determined with the CX diagnostics from the core to the pedestal top (see figure 4). However, it is reasonable to assume $T_i^{\text{sep}} > T_e^{\text{sep}}$. In principle, this can affect the PB stability results. For this reason, a sensitivity test has been done for the reference pulses. In the sensitivity tests, T_i^{sep} has been increased from 100 eV up to 70% of the pedestal top temperature and the effects on both α_{exp} and α_{crit} have been estimated. The effect of T_i^{sep} is negligible for both α_{exp} and α_{crit} in pulse #96202. As shown in figure 2, this pulse has relatively low separatrix density, so a change in T_i^{sep} has a minor effect of the maximum total pressure gradient. On the other hand, the effect of T_i^{sep} is slightly stronger in #96201. In this case, the separatrix density is higher, and the increase in T_i^{sep} leads to a $\approx 15\%$ – 20% reduction in both α_{exp} and α_{crit} . α_{exp} is reduced because the higher T_i^{sep} leads to a lower total pressure gradient. In turn, the change in the total pressure gradient affects also the PB stability leading to the reduction in α_{crit} .

However a variation of 15%–20% will not change the conclusion of the present work. More importantly, the reductions in α_{exp} and α_{crit} in #96201 compensate each other, so the change in $\alpha_{\text{crit}}/\alpha_{\text{exp}}$ with $T_{\text{i}}^{\text{sep}}$ is negligible.

The effect of $T_{\text{e}}^{\text{sep}}$ on pedestal stability has been discussed in several earlier works [35, 43]. In particular, it was shown that a reasonable uncertainty in $T_{\text{e}}^{\text{sep}}$ does not affect significantly the PB stability conclusions [24].

3.2.2. Resistive peeling-ballooning stability. The effect of resistivity on the PB stability is tested with the linear resistive MHD stability code CASTOR [44]. The workflow is similar to the one described for the ideal MHD.

3.2.3. Pedestal pressure predictive modelling. The pedestal pressure height is predicted with Europol code [28, 45] which implements the EPED1 model [46]. The model is based on the assumption that the ELMs are triggered when the PB stability boundary is reached and on the assumption that the pedestal transport is due to kinetic ballooning modes (KBM) driven turbulence. This second assumption is implemented via the expression:

$$w_{\text{pe}} = 0.076 \sqrt{\beta_{\theta}^{\text{ped}}}, \quad (2)$$

where $\beta_{\theta}^{\text{ped}}$ is the poloidal beta at the pedestal top. The more recent version of the model, EPED1.6, allows a variation of the coefficient 0.076 which is determined using a ‘ballooning critical pedestal’ technique for the KBM transport [47]. This second version is not investigated further since, as presented in section 7, the KBMs do not seem to be the dominant micro-instabilities in the plasmas studied in this work.

The Europol code uses HELENA for the equilibrium and ELITE for the PB stability. The predictions are therefore based on ideal MHD. The key input parameters are I_{p} , B_{t} , the plasma shape, β_{N} , Z_{eff} , $n_{\text{e}}^{\text{ped}}$ and $n_{\text{e}}^{\text{pos}}$. The code assumes $w_{\text{ne}} = w_{\text{T_e}}$. The outputs are the pedestal pressure height and the pedestal pressure width.

3.2.4. Separatrix density modelling. The modelling related to the understanding of the qualitative behaviour of $n_{\text{e}}^{\text{sep}}$ is done with JINTRAC [48]. JINTRAC is an integrated code suite that can include several physics-modules. In the modelling done in this work, JINTRAC has used EDGE2D-EIRENE [49–51] for the scrape-off layer (SOL) transport and for the neutral transport, JETTO [52] for the core transport (using a Bohm-gyroBohm model) and a simple model that triggers the ELMs in the pedestal (when the pressure gradient reaches a critical threshold, ∇p_{crit}). In the present JINTRAC modelling, the profiles evolve between ELMs assuming prescribed transport coefficients profiles with ELMs simulated by suddenly increasing the transport coefficients when the ∇p_{crit} is reached. The input parameters most relevant for this work are the radial profiles of the transport coefficients, the gas rate, the input power and ∇p_{crit} . The value of ∇p_{crit} is determined in order to have an ELM frequency comparable to the experimental value. The time evolution of the electron density and

temperature profiles are among the outputs of JINTRAC. In this work we will focus on the pre-ELM profiles.

3.2.5. Turbulent transport in the pedestal. The microinstabilities and the turbulent transport in the pedestal region have been investigated with the gyrokinetic code GENE [53, 54] with local linear and local non-linear simulations. More details will be provided in section 7.

4. Correlation of the pedestal pressure with $n_{\text{e}}^{\text{sep}}$ and with $n_{\text{e}}^{\text{sep}}/n_{\text{e}}^{\text{ped}}$

Experimental correlations between pedestal pressure and separatrix density have been observed already in earlier works. Negative correlations between pedestal pressure and separatrix density have been observed in Alcator C-Mod, AUG and JET. In Alcator C-Mod, the correlation was observed using the normalized separatrix density (to either the line average density or the pedestal density) [13, 55]. In AUG and JET the correlation was observed using the absolute separatrix density [11, 24]. Before proposing a mechanism to explain these negative correlations, it is important to identify if the relevant parameter is $n_{\text{e}}^{\text{sep}}$ or $n_{\text{e}}^{\text{sep}}/n_{\text{e}}^{\text{ped}}$.

The difference between using $n_{\text{e}}^{\text{sep}}$ or $n_{\text{e}}^{\text{sep}}/n_{\text{e}}^{\text{ped}}$ is shown in figures 6(a) and (b) for the constant β_{N} datasets and for the extended low- δ dataset. Figure 6(a) shows the correlation between $p_{\text{e}}^{\text{ped}}$ and $n_{\text{e}}^{\text{sep}}$, while figure 6(b) between $p_{\text{e}}^{\text{ped}}$ and $n_{\text{e}}^{\text{sep}}/n_{\text{e}}^{\text{ped}}$. The extended low- δ dataset (grey squares) shows a correlation in both cases, albeit slightly clearer using $n_{\text{e}}^{\text{sep}}/n_{\text{e}}^{\text{ped}}$. On the other hand, the constant β_{N} datasets (circles and triangles) show a weak correlation between $p_{\text{e}}^{\text{ped}}$ and $n_{\text{e}}^{\text{sep}}$. This is particularly evident for the subsets at $\beta_{\text{N}} = 1.9$ and $\beta_{\text{N}} = 1.5$. Instead, the correlation is clear when using $n_{\text{e}}^{\text{sep}}/n_{\text{e}}^{\text{ped}}$ (figure 6(b)). Note that in figure 6(b) no systematic difference is present between the subsets with the horizontal and corner configurations (empty and full symbols respectively). This suggests that the difference in the performance of the two configurations (see for example, [7, 24, 56]) is due to the different $n_{\text{e}}^{\text{sep}}/n_{\text{e}}^{\text{ped}}$ produced by the different pumping efficiency and/or recycling (as also discussed in [24]). Since, no systematic difference between horizontal and corner configurations is observed in figure 6(b), hereafter the role of the divertor configuration is not discussed further.

The correlation between $p_{\text{e}}^{\text{ped}}$ and $n_{\text{e}}^{\text{sep}}/n_{\text{e}}^{\text{ped}}$ is robust and can be observed also with other plasma currents. As an example, figure 6(c) shows the correlation between $p_{\text{e}}^{\text{ped}}$ and $n_{\text{e}}^{\text{sep}}/n_{\text{e}}^{\text{ped}}$ in JET-ILW for all low- δ deuterium plasmas up to 2.5 MA.

These results suggest that the most relevant parameter for describing pedestal physics is $n_{\text{e}}^{\text{sep}}/n_{\text{e}}^{\text{ped}}$ rather than $n_{\text{e}}^{\text{sep}}$. Hereafter the work will focus on the correlation between $p_{\text{e}}^{\text{ped}}$ and $n_{\text{e}}^{\text{sep}}/n_{\text{e}}^{\text{ped}}$. Of course, the pedestal pressure is correlated also to other parameters, such as pedestal gradient and pedestal positions. However, the gradient is determined by the pedestal stability and pedestal position is strongly correlated to $n_{\text{e}}^{\text{sep}}/n_{\text{e}}^{\text{ped}}$ (as shown in section 5). So, no empirical correlation between $p_{\text{e}}^{\text{ped}}$ with gradient and position will be discussed.

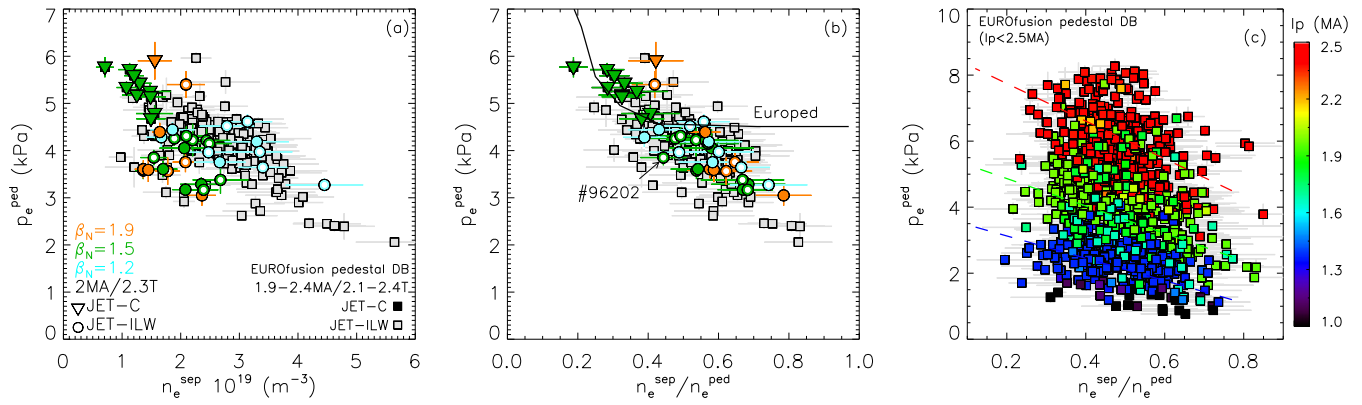


Figure 6. Correlation between the pedestal pressure with the separatrix density (a) and with the separatrix density normalized to the pedestal density (b). The circles (JET-ILW) and the triangles (JET-C) show the three subsets at constant β_N . The squares show the wider dataset extracted from the EUROfusion pedestal database. The continuous line in frame (b) shows the pedestal predictions with Europed discussed in section 6. Frame (c) shows the same correlation using all JET-ILW deuterium plasmas with low- δ and I_p up to 2.5 MA. The dashed lines in frame (c) show the linear regressions for subsets at 1.4 MA (blue), 2 MA (green) and 2.5 MA (red).

5. Link between $n_e^{\text{sep}}/n_e^{\text{ped}}$, n_e^{pos} and gas rate: experimental results and qualitative modelling

Experimentally, the increase of $n_e^{\text{sep}}/n_e^{\text{ped}}$ in figures 6(a) and (b) has been achieved by increasing the gas rate and/or by changing the strike point position. Modelling the effect of the strike point position on n_e^{sep} is beyond the scope of this work. The goals of the section are to (1) describe the experimental correlations between $n_e^{\text{sep}}/n_e^{\text{ped}}$, n_e^{pos} and gas rate and (2) present a modelling that can (a) qualitatively reproduce the experimental correlations and (b) provide its qualitative explanation.

To date, the main SOL modelling that includes a description of the behaviour of the density position in H-mode plasmas has been done in AUG [57], where it is shown that n_e^{pos} is strongly affected by the presence of a high density front in the high field side SOL region (high field side high density, HFSHD). Study of the SOL density in H-mode plasma have been done also in DIII-D [22, 23], where the focus was related mainly to the behaviour of n_e^{sep} . In JET-ILW, extensive SOL modelling has been typically done in L-mode plasmas, where the experimental positive correlation between n_e^{sep} and Γ_{D2} was well reproduced [58–60]. The modelling of the links between $n_e^{\text{sep}}/n_e^{\text{ped}}$, n_e^{pos} and Γ_{D2} in JET H-mode plasmas has not been done yet.

Recent experimental results on the correlation between n_e^{sep} with the SOL and the target conditions in JET-ILW can be found in [61, 62]. These results have been obtained in plasmas similar to those discussed in this work, with same I_p , B_t , plasma shape, with similar power but with scans over a slightly wider range in gas rate than in the present constant β_N datasets. The HFSHD was observed in the past in some JET-ILW plasmas [63], but the results discussed in [61, 62] show that the HFSHD does not seem to play a significant role in determining n_e^{sep} in the dataset used in this work. So, it is useful to investigate if another mechanism can explain the variation of $n_e^{\text{sep}}/n_e^{\text{ped}}$ and n_e^{pos} in JET-ILW.

The experimental density profiles for the reference pulses #96201 and #96202 are shown in figure 7(a). Pulse #96201

has higher gas rate and is characterized by higher n_e^{ped} and higher n_e^{sep} than #96202. The difference with gas rate in the density is stronger at the separatrix than at the pedestal top, so #96201 has also higher $n_e^{\text{sep}}/n_e^{\text{ped}}$ than #96202, see figure 7(b). Another important difference is that n_e^{pos} is more outwards in #96201. This was shown also in figure 2(e), where n_e^{pos} was determined from the position of the maximum gradient.

The effect of the gas rate on the pedestal density profile has been modelled with the JINTRAC code suit (see section 3.2 for details). The modelling started by using the low gas rate pulse #96202 as reference. Prescribed transport coefficient profiles have been assumed in the pedestal and in the SOL. In the pedestal region (defined as $3.81 \text{ m} < R < 3.845 \text{ m}$), the particle transport has been set to $D_e = 0.05 \text{ m}^2 \text{ s}^{-1}$ and the heat transport to $\chi_e = 0.35 \text{ m}^2 \text{ s}^{-1}$. In the SOL region (defined as $R > 3.845 \text{ m}$), the transport coefficients have been set to $D_e = 0.35 \text{ m}^2 \text{ s}^{-1}$ and $\chi_e = 0.9 \text{ m}^2 \text{ s}^{-1}$. In the core, the transport is determined with a Bohm-gyroBohm model. In the modelling, the ELMs are triggered when a critical pressure gradient (∇p_{crit}) is reached. When the ELM is triggered, the transport coefficients are increases to $\approx 5 \text{ m}^2 \text{ s}^{-1}$ for 1 ms (with a 0.1 ms ramp-up and 0.1 ms ramp-down). The transport coefficients and ∇p_{crit} have been selected to have a reasonable agreement with the experimental density profile and the experimental f_{ELM} of pulse #96202 (40 Hz). The experimental gas rate and the input power of pulse #96202 have been used, $\Gamma_{D2} = 0.75 \times 10^{22} \text{ (e s}^{-1}\text{)}$ and $P_{\text{NBI}} = 14 \text{ MW}$ respectively. To have a consistent comparison with the experimental profiles, the following results are based on the pre-ELM modelled profiles. The pre-ELM modelled density is shown in figure 7(c) with the blue line. The modelled n_e^{pos} has been determined by fitting the simulated pre-ELM density with the mtanh function.

Then, starting from this reference case, the modelling has been repeated by changing the gas rate, while keeping the transport coefficients constant. Several approaches have been used for ∇p_{crit} and the input power. In the first set of gas scan simulations, ∇p_{crit} has been changed to mimic the experimental increase of f_{ELM} with the gas rate (up to 80–100 Hz) and the input power has been increased as in the experiment (up

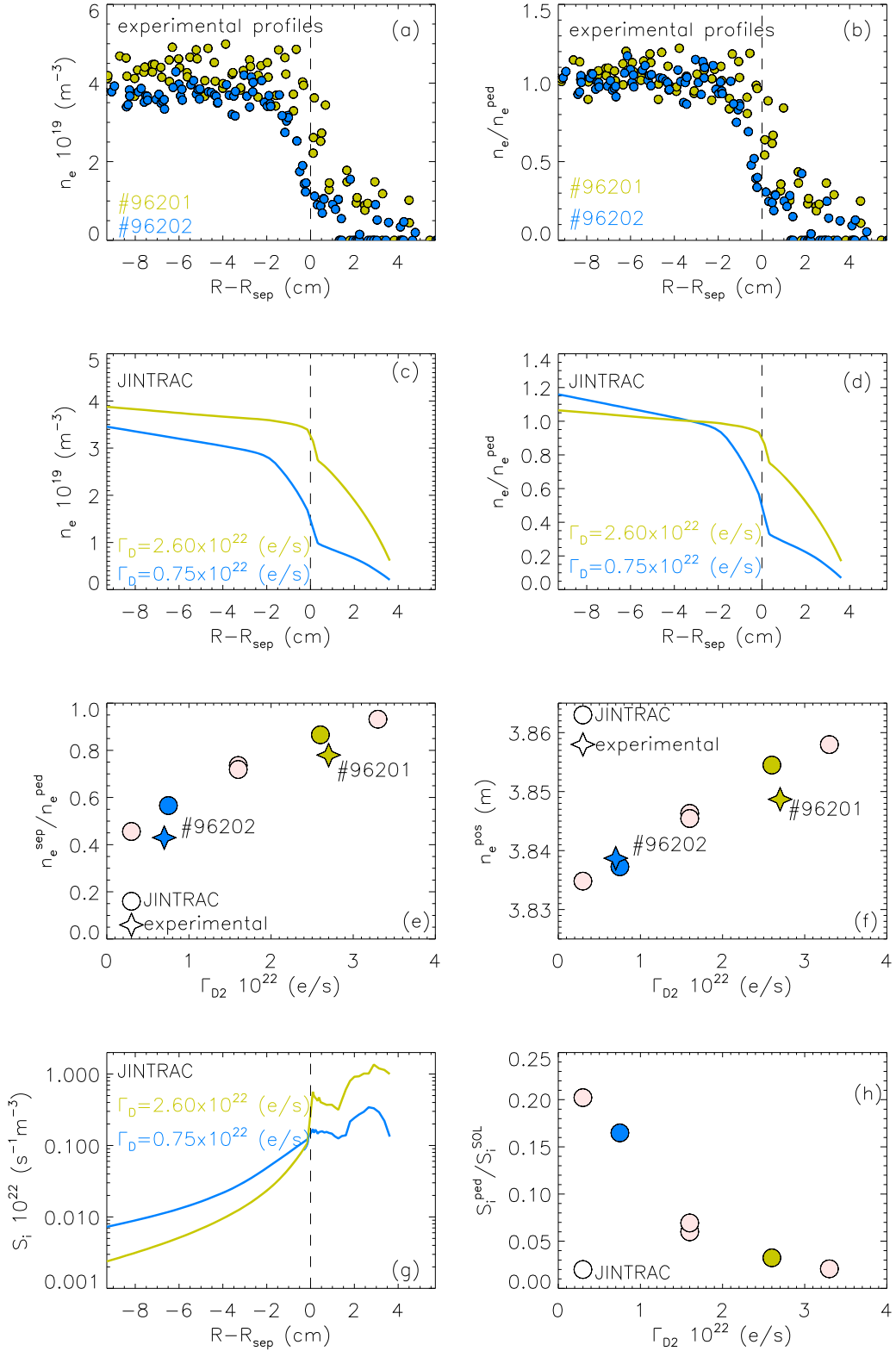


Figure 7. Frame (a) shows experimental pre-ELM density profiles for the reference pulses #96201 and #96202. Frame (b) shows the profiles normalized to the pedestal density. Frames (c) and (d) show the modelled pre-ELM profile for the reference case (blue) corresponding to the Γ_{D2} of #96202 and using higher gas rate (yellow) corresponding to #96201. Frames (e) and (f) show the correlation with gas rate of $n_e^{\text{sep}}/n_e^{\text{ped}}$ and n_e^{pos} for the modelled data (circles) and the reference pulses (stars). Frame (g) shows the radial profile of the ionization rates. Frame (h) shows the correlation between $S_i^{\text{ped}}/S_i^{\text{SOL}}$ and gas rate.

to 18 MW). In the second set of simulations, ∇p_{crit} has been kept constant to the value of the reference case. In the third set of simulation, the input power has been kept constant to the reference case. These approaches have produced similar results in terms of simulated pre-ELM $n_e^{\text{sep}}/n_e^{\text{ped}}$ and n_e^{pos} . To be consistent with the experimental case, the results of the first approach are shown in figure 7. Figures 7(c) and (d) show with the yellow line the pre-ELM density profile modelled with $\Gamma_{\text{D2}} = 2.6 \times 10^{22}$ (e s^{-1}), corresponding to the gas rate used in #96201, to be compared with the reference modelled profile (blue line, $\Gamma_{\text{D2}} = 0.75 \times 10^{22}$ (e s^{-1}), corresponding to the rate of #96202). The profile modelled with high Γ_{D2} is characterized by n_e^{sep} and $n_e^{\text{sep}}/n_e^{\text{ped}}$ higher than the low Γ_{D2} case. In the high Γ_{D2} case, the region with the highest density gradient is located outside the separatrix, while this region is located mainly inside the separatrix in the low Γ_{D2} case. This behaviour is qualitatively similar to a change in the density profile position. The modelling results of the entire gas scan are reported in figures 7(e) and (f) with circles. A clear positive correlation between $n_e^{\text{sep}}/n_e^{\text{ped}}$ and Γ_{D2} and between n_e^{pos} and Γ_{D2} is present. For comparison, the stars in figures 7(e) and (f) show the experimental values corresponding to the reference pulses. Experimental data and simulations show a reasonable agreement.

The reason for the increase of $n_e^{\text{sep}}/n_e^{\text{ped}}$ with increasing Γ_{D2} is investigated in figures 7(g) and (h), where the modelled ionization rate S_i is shown. Figure 7(g) shows the radial profiles at the midplane of the modelled S_i for the low and high gas cases. The increase of the gas rate leads to a strong increase in the ionization rate outside the separatrix. This leads to the increase in n_e^{sep} . Instead, inside the separatrix S_i decreases with increasing Γ_{D2} . This suggests that the SOL becomes opaque at high gas rate, due to the neutrals which cannot easily move inside the separatrix. As a consequence, the height of the pedestal density has only a small increase with increasing Γ_{D2} . This leads to the increase of $n_e^{\text{sep}}/n_e^{\text{ped}}$ with increasing Γ_{D2} . Effectively, this change can be interpreted as a radial outward shift of the density profile. The behaviour of the ionization rate profile is further discussed in figure 7(h), where the ratio $S_i^{\text{ped}}/S_i^{\text{SOL}}$ is shown for the modelled gas scan (with S_i^{ped} and S_i^{SOL} represents S_i determined at the pedestal top and in the SOL, respectively). $S_i^{\text{ped}}/S_i^{\text{SOL}}$ clearly decreases with increasing gas rate, further strengthening the idea of increasing SOL opacity with increasing Γ_{D2} .

The modelling has been repeated using constant ∇p_{crit} and constant input power, producing results consistent to those shown in figure 7. Therefore, it is possible to conclude that the variation of in $n_e^{\text{sep}}/n_e^{\text{ped}}$ and in n_e^{pos} in the modelling is due to the gas rate and not to variation in f_{elm} or in the power.

The modelling discussed in figure 7 is very similar to results obtained in Alcator C-Mod [64] where it was observed (i) the S_i^{SOL} increase and (ii) the S_i^{ped} decrease with increasing gas rate. In C-mod, these effects led to a significant reduction of the neutral penetration producing a strong increase of the ion separatrix density and a much weaker increase of the ion pedestal density. In a recent work, this behaviour has been linked to the high neutral opacity that can characterize Alcator C-Mod plasmas [65].

It must be highlighted that the goal of the modelling described in figure 7 is not to obtain a quantitative agreement between the modelled density profiles and the experimental profiles, but only to provide a possible qualitative understanding of the correlations between $n_e^{\text{sep}}/n_e^{\text{ped}}$ and Γ_{D2} and between n_e^{pos} and Γ_{D2} . A quantitative agreement would require at least two steps. (1) A better fine tuning of the transport coefficients, in order to obtain a better agreement with the experimental profiles of the reference case. (2) An increase of the transport coefficients with increasing the gas rate. In fact, the increasing Γ_{D2} is likely to produce an increase in the transport via an increased $n_e^{\text{sep}}/n_e^{\text{ped}}$ (as discussed in [66] and investigated in section 7). This would require a self-consistent modelling in which the transport coefficients are determined both in the pedestal and in the SOL by turbulent transport codes such as GENE [53, 67] for the pedestal and TOKAM3X [68] for SOL. This cannot be done in the present work, so we cannot exclude that the increase in $n_e^{\text{sep}}/n_e^{\text{ped}}$ and in n_e^{pos} with the gas rate is related also to a change in the transport coefficients.

The modelled results and the experimental data discussed in figure 7 suggest that a positive correlation between $n_e^{\text{sep}}/n_e^{\text{ped}}$ and n_e^{pos} is present. Experimentally, this result is very robust and is valid for all low- δ JET-ILW plasma, as shown in figure 8. Figure 8(a) shows the correlation between n_e^{pos} and $n_e^{\text{sep}}/n_e^{\text{ped}}$ for the constant β_N datasets (circles and triangles), for the extended low- δ dataset (squares) and for the modelling results presented in figure 7 (stars). All the datasets show a positive correlation, with no systematic differences. The increase in $n_e^{\text{sep}}/n_e^{\text{ped}}$ is clearly correlated to the outward shift of the density profile. Moreover, figure 8(a) shows that JET-C plasmas tend to have lower $n_e^{\text{sep}}/n_e^{\text{ped}}$ and more inward n_e profiles than JET-ILW plasmas. The same conclusion can be obtained when evaluating the density position in real space (along the line of sight of the TS diagnostic), as shown in figure 8(b) for the constant β_N datasets. An example is shown in figure 8(c) for two extreme cases, a JET-ILW pulse with high $n_e^{\text{sep}}/n_e^{\text{ped}}$ (#96208) and a JET-C pulse with low $n_e^{\text{sep}}/n_e^{\text{ped}}$ (#79523).

Given the strong correlation between $n_e^{\text{sep}}/n_e^{\text{ped}}$ and n_e^{pos} shown in figure 8(a), the pedestal simulations of the following sections have been performed by modelling the variation of $n_e^{\text{sep}}/n_e^{\text{ped}}$ with an artificial radial shifts of the density profile.

6. Role of n_e^{pos} in the pedestal performance and Europol modelling

Recent studies in AUG, JET-ILW and TCV have highlighted that n_e^{pos} can affect the pedestal performance via an effect on the PB stability [11, 17, 18, 69]. The outward radial shift of the density leads to the outward shift of the pedestal pressure which destabilizes the PB modes and reduces the pedestal pressure height. This is in agreement with earlier results obtained in Alcator C-Mod, DIII-D and NSTX [70–74].

The strong correlation between $n_e^{\text{sep}}/n_e^{\text{ped}}$ and n_e^{pos} shown in figure 8(a) suggests the change in n_e^{pos} can explain, at least in part, the degradation of the pedestal pressure with increasing $n_e^{\text{sep}}/n_e^{\text{ped}}$ shown in figure 6(b). The first part of this section tests this hypothesis using the Europol code and shows that

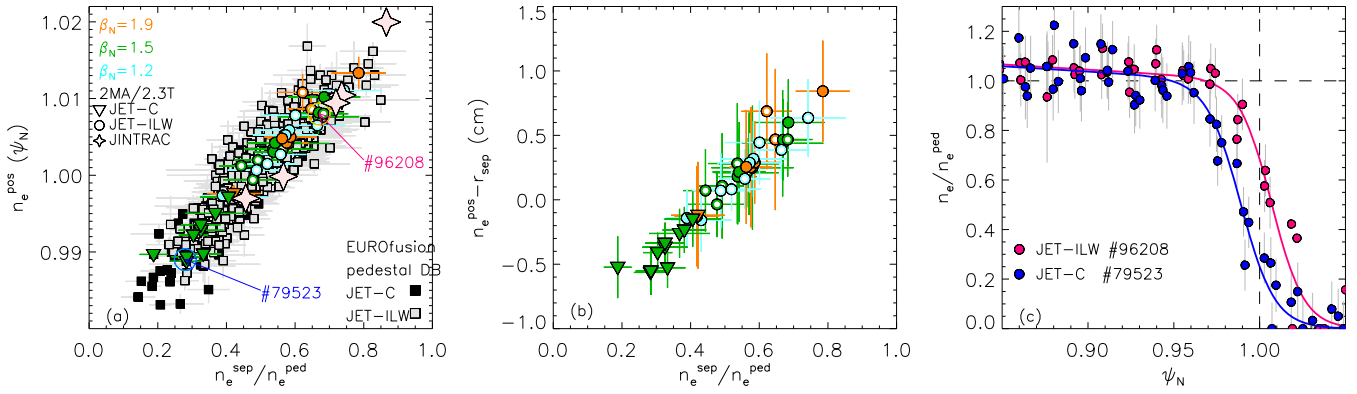


Figure 8. (a) Correlation between n_e^{pos} (in normalized poloidal flux units) and $n_e^{\text{sep}}/n_e^{\text{ped}}$ for the datasets at constant β_N and for the extended low- δ dataset. (b) Same correlation of frame (a) but evaluated in real space, along the line of sight of the TS diagnostic. (c) Comparison of a JET-ILW pre-ELM density profile at high $n_e^{\text{sep}}/n_e^{\text{ped}}$ and a JET-C density profile at low $n_e^{\text{sep}}/n_e^{\text{ped}}$.

the effect of n_e^{pos} can explain the experimental trend only at low $n_e^{\text{sep}}/n_e^{\text{ped}}$.

6.1. Effect of n_e^{pos} on p_e^{ped}

The hypothesis that a change in n_e^{pos} can explain the correlation between p_e^{ped} and $n_e^{\text{sep}}/n_e^{\text{ped}}$ has been tested with the Europed code [28]. Initially, the modelling has been done for the JET-ILW reference case #96202 (low gas, $\beta_N = 1.5$, $n_e^{\text{sep}}/n_e^{\text{ped}} \approx 0.4$), producing a reasonable agreement within 20% with the experimental data, $p_e^{\text{crit}} = 4.5$ kPa and $p_e^{\text{ped}} = (3.8 \pm 0.2)$ kPa. Then, starting from the reference case, the modelling is repeated by shifting the density profile inwards and outwards, in order to mimic the variation in $n_e^{\text{sep}}/n_e^{\text{ped}}$, while keeping all other input parameters constant. This is a reasonable approach as long as β_N is constant. In fact, the Europed modelling of the entire $\beta_N = 1.5$ dataset would require the same input parameters, apart n_e^{pos} . The scan in the position of the density profiles has been such to change $n_e^{\text{sep}}/n_e^{\text{ped}}$ in the range $n_e^{\text{sep}}/n_e^{\text{ped}} \approx 0.1$ –0.9. The predicted pedestal pressure is shown in figure 6(b) with the black continuous line.

The reduction of $n_e^{\text{sep}}/n_e^{\text{ped}}$ below 0.4 leads to a clear increase in the predicted pedestal height. Below $n_e^{\text{sep}}/n_e^{\text{ped}} = 0.4$, the experimental trend between p_e^{ped} and n_e^{pos} is well reproduced by Europed. Moreover, starting from the JET-ILW reference case #96202, the modelling reproduces the high pedestal pressure observed in the JET-C dataset. This suggests that the low $n_e^{\text{sep}}/n_e^{\text{ped}}$ and the low n_e^{pos} typical of JET-C are key parameters in explaining the difference in the pedestal performance between JET-C and JET-ILW. This is further discussed in section 10.

On the contrary, the increase of $n_e^{\text{sep}}/n_e^{\text{ped}}$ above 0.4 does not lead to any significant change in the predicted pedestal pressure. The experimental negative correlation between p_e^{ped} and $n_e^{\text{sep}}/n_e^{\text{ped}}$ is not reproduced by the model for $n_e^{\text{sep}}/n_e^{\text{ped}} > 0.4$.

The different behaviour of the predicted pressure at low and high $n_e^{\text{sep}}/n_e^{\text{ped}}$ is due to the link between n_e^{pos} and p_e^{pos} . When n_e^{pos} is near T_e^{pos} (which occurs at low $n_e^{\text{sep}}/n_e^{\text{ped}}$), a change

in n_e^{pos} has a significant effect on the pressure position. On the contrary, when n_e^{pos} is significantly more outward than T_e^{pos} (which occurs at high $n_e^{\text{sep}}/n_e^{\text{ped}}$), the region with steep ∇n_e is located in a radial range where the temperature is very low. In this radial range, a change in n_e^{pos} has a negligible effect on p_e^{pos} . This is shown in figure 9. Figure 9(a) shows the temperature profile (grey line) and the density profile (black line) for the reference shot #96202. The coloured lines in figure 9(a) show the density profiles radially shifted inwards and outwards. Figure 9(b) shows the corresponding pressure profiles determined from the product of the T_e and n_e profiles. The pressure profiles move radially outwards when the n_e profile is shifted outwards from its innermost radial position, i.e. from the violet/blue profiles at $n_e^{\text{sep}}/n_e^{\text{ped}} \approx 0.1$ till the green profiles at $n_e^{\text{sep}}/n_e^{\text{ped}} \approx 0.4$. However, further outwards radial shifts of the n_e profile have a minimal effect on the pressure. This behaviour is summarized in figure 9(c), where the correlation between p_e^{pos} and $n_e^{\text{sep}}/n_e^{\text{ped}}$ is shown. p_e^{pos} increases till $n_e^{\text{sep}}/n_e^{\text{ped}} \approx 0.4$, while it remains constant for $n_e^{\text{sep}}/n_e^{\text{ped}} > 0.4$. This behaviour is consistent with the experimental results for the two reference pulses, #96201 and #96202. As shown in figure 2(e) and in figure 2(f), the high gas rate pulse #96201 has higher n_e^{pos} than the low gas pulse #96202, however, the two pedestals have the same pressure position.

The results of figures 6(b) and 9(c) show that the correlation between p_e^{ped} and $n_e^{\text{sep}}/n_e^{\text{ped}}$ can be explained by a change in the pressure position only for $n_e^{\text{sep}}/n_e^{\text{ped}} < 0.4$. Before investigating which mechanism might be relevant at higher $n_e^{\text{sep}}/n_e^{\text{ped}}$, it is useful to identify if the failure in predicting p_e^{ped} at $n_e^{\text{sep}}/n_e^{\text{ped}} > 0.4$ is due to a problem in the predicted Europed pedestal pressure width or in the predicted Europed pedestal pressure gradient.

6.2. Problems in the Europed modelling at high $n_e^{\text{sep}}/n_e^{\text{ped}}$

Figure 10 investigates the pedestal width behaviour. Figure 10(a) shows the experimental correlation between w_{p_e} and $n_e^{\text{sep}}/n_e^{\text{ped}}$ for the constant β_N datasets. The JET-ILW subsets have higher $n_e^{\text{sep}}/n_e^{\text{ped}}$ and wider w_{p_e} than the JET-C subsets. The grey area shows the range of the pedestal width predicted

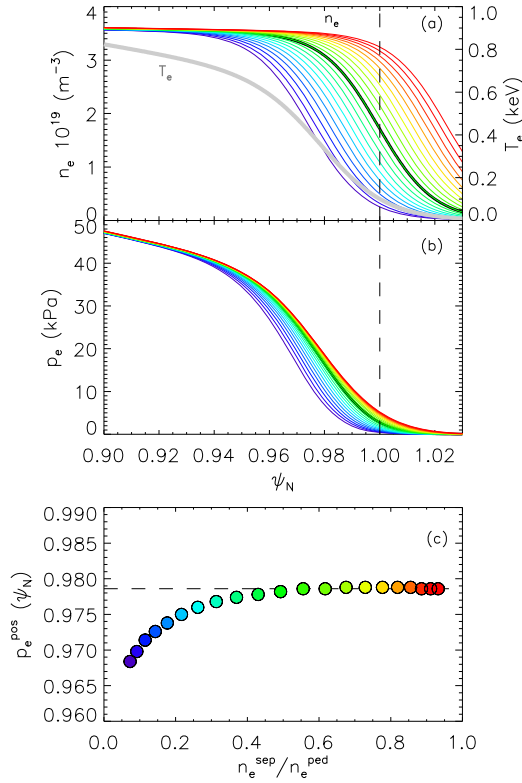


Figure 9. (a) T_e and n_e profiles for #96202 (grey and black lines respectively). The coloured lines show the n_e profile radially shifted inwards and outwards from the experimental profile. (b) Corresponding p_e profile, determined from the product of T_e and n_e . (c) Corresponding correlation between p_e^{pos} and $n_e^{\text{sep}}/n_e^{\text{ped}}$.

by Europol, see expression (2). Europol tends to overestimate the pedestal width at $n_e^{\text{sep}}/n_e^{\text{ped}} < 0.4$ and to underestimate the width at $n_e^{\text{sep}}/n_e^{\text{ped}} > 0.4$. In other works, different results have been obtained when looking at the width in ψ_N space or real space. For example, in AUG the correlation between width and $\beta_{\theta}^{\text{ped}}$ was observed only in ψ_N space and not in real space [70]. It is worth to notice that the correlation of figure 10(a) is valid still in real space, as shown in figure 10(b). The comparison between modelled and experimental w_{pe} is further investigated in figure 10(c) where the correlation between w_{pe} and $\beta_{\theta}^{\text{ped}}$ is shown. The dashed line shows the EPED1 width determined with expression (2). The constant β_N datasets and the extended low- δ dataset do not show the clear positive correlation between w_{pe} and $\beta_{\theta}^{\text{ped}}$ that is predicted by EPED1. Only the JET-C subset seems to have a positive correlation between w_{pe} and $\beta_{\theta}^{\text{ped}}$, however the EPED1 predictions overestimate the experimental widths by approximately 50%. We should note that the disagreement between experimental width and EPED1 predicted width is not related to the definition of w_{pe} used in this work. Reference [24] has shown that similar conclusion are obtained using other pedestal width definitions.

Figure 11 investigates the pedestal gradient behaviour. Figure 11(a) shows the experimental correlation between the normalized pedestal pressure gradient (α_{exp}) and $n_e^{\text{sep}}/n_e^{\text{ped}}$ for the constant β_N datasets. A clear negative correlation is

present. The continuous black line shows the pressure gradient predicted by Europol (using the same modelling discussed in figure 6(b)). The predictions are rather good for the JET-C subset. On the other hand, Europol tends to overestimate the pressure gradient for the JET-ILW subset. In particular, at high $n_e^{\text{sep}}/n_e^{\text{ped}}$ the difference is up to a factor 2. This is because the Europol modelling assumes that the ELMs are triggered when the ideal MHD boundary is reached. However, as discussed in the introduction, at high P_{sep} and high Γ_{D2} the JET-ILW pedestals are not limited by ideal MHD. Figure 11(b) shows the ratio $\alpha_{\text{crit}}/\alpha_{\text{exp}}$ versus $n_e^{\text{sep}}/n_e^{\text{ped}}$. α_{crit} has been determined with the ideal PB stability analysis described in section 3.2.1 using ELITE and using the experimental pre-ELM profiles as input. A value of $\alpha_{\text{crit}}/\alpha_{\text{exp}} \approx 1$ implies that the ELMs are triggered when the pedestal reaches ideal PB boundary, a higher value implies that ideal PB stability is not the cause of the ELMs. Figure 11(b) shows that $\alpha_{\text{crit}}/\alpha_{\text{exp}} < 1.3$ at low separatrix density ($n_e^{\text{sep}}/n_e^{\text{ped}} < 0.4$), so the ELMs are due to ideal PB modes. It is worth to highlight that the JET-C subset has $\alpha_{\text{crit}}/\alpha_{\text{exp}} < 1.2$. Instead, the ratio $\alpha_{\text{crit}}/\alpha_{\text{exp}}$ can increase up to ≈ 2 at $n_e^{\text{sep}}/n_e^{\text{ped}} > 0.4$. Most of the data in the JET-ILW subset have $\alpha_{\text{crit}}/\alpha_{\text{exp}} > 1.3$, so they have a pedestal in which the ELMs are triggered before the ideal PB stability boundary is reached. Ideal PB modes are not the cause of the ELMs in these plasmas, which explains why Europol overpredicts the pressure gradient at $n_e^{\text{sep}}/n_e^{\text{ped}} > 0.4$.

7. Effect of $n_e^{\text{sep}}/n_e^{\text{ped}}$ on microinstabilities and turbulent transport

The disagreement between the Europol pedestal predictions and the experimental results at $n_e^{\text{sep}}/n_e^{\text{ped}} > 0.4$ are related not only to p_e^{ped} , but also to the pedestal width and the pressure gradient.

In general, both the behaviours of the pedestal width and of the pedestal gradient can be related to the pedestal transport. Simulations done with GENE [66, 67, 75] and GS2 [18] suggest that the increase of the separatrix density might lead to an increase in the turbulent transport. This is because an increase in $n_e^{\text{sep}}/n_e^{\text{ped}}$ can affect the density gradient scale length L_{n_e} and hence the parameter η_e (the ratio between density and temperature gradient scale lengths, $\eta_e = L_{n_e}/L_{T_e}$) which can affect turbulent transport.

One of the EPED1 assumptions is that the pedestal transport is driven by KBMs. Indeed, observations consistent with KBMs have been reported [76–78]. However, this is not a general conclusion and, depending on the plasma parameters and/or the radial position under investigation, other microinstabilities (such as microtearing modes, electron temperature gradient modes, ion temperature gradient modes) have been observed in the pedestal, both experimentally and in modelling [66, 75, 79–84].

This section describes the link between $n_e^{\text{sep}}/n_e^{\text{ped}}$ with microinstabilities and turbulent transport in the plasmas presented in section 2. It will be shown that slab-ETG (electron temperature gradient) instabilities dominate the transport in the middle of the pedestal of these plasmas.

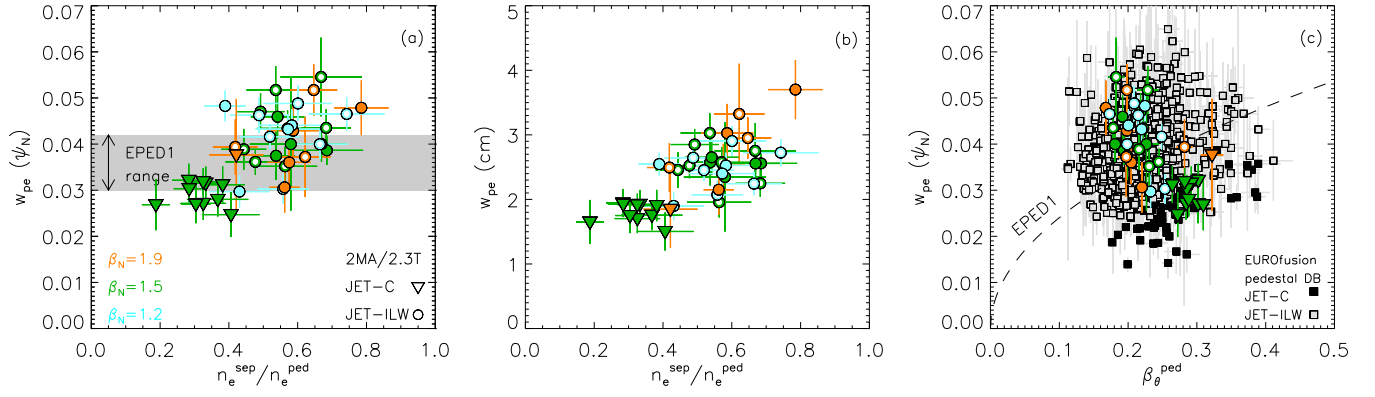


Figure 10. (a) Correlation between w_{pe} (in normalized poloidal flux units) and n_e^{sep}/n_e^{ped} . The grey area highlights the range of pedestal widths predicted by EPED1. (b) Same correlation of frame (a) but with the pedestal width determined in real space, along the TS line of sight. (c) Correlation between w_{pe} and β_{θ}^{ped} . The dashed line shows the EPED1 prediction based on KBM transport, see expression (2).

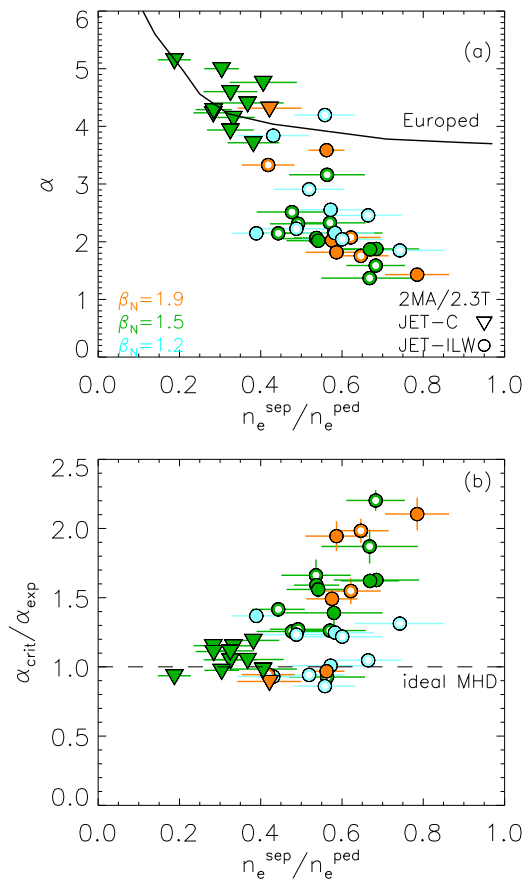


Figure 11. (a) Correlation between the normalized pressure gradient and n_e^{sep}/n_e^{ped} for the datasets at constant β_N . The black line shows the Europol predictions corresponding to the modelling of figure 6(b). (b) Correlation between $\alpha_{crit}/\alpha_{exp}$ and n_e^{sep}/n_e^{ped} .

7.1. Experimental correlations between $\nabla n_e/n_e$, η_e and n_e^{sep}/n_e^{ped}

The experimental correlations between n_e^{sep}/n_e^{ped} with $1/L_{n_e} = \nabla n_e/n_e$ and η_e are shown in figure 12. $\nabla n_e/n_e$ has been evaluated at $\psi_N = 1$ (to have a direct link with n_e^{sep}/n_e^{ped}) and for simplicity ∇n_e has been calculated as $dn_e/d\psi_N$. The correlation between n_e^{sep}/n_e^{ped} and $\nabla n_e/n_e$ is

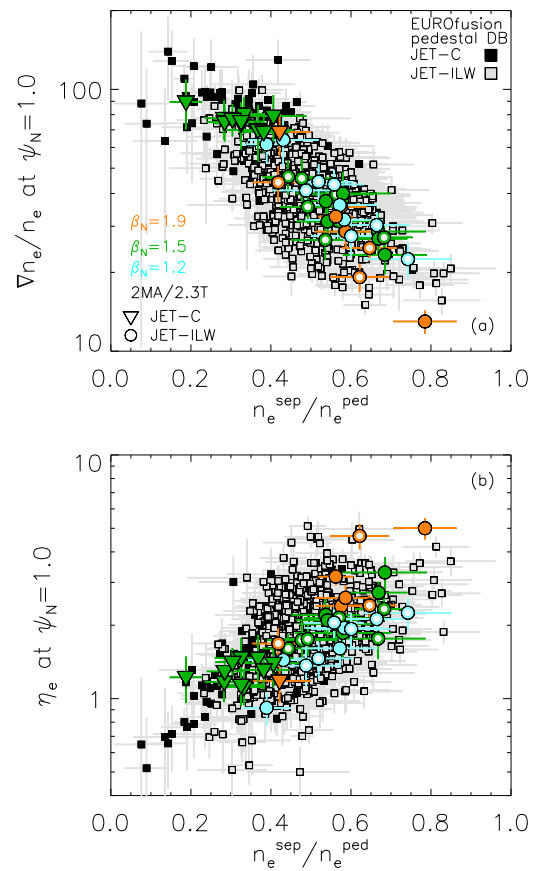


Figure 12. Correlations of (a) $\nabla n_e/n_e$ and (b) η_e versus n_e^{sep}/n_e^{ped} for the datasets at constant β_N and for the extended low- δ dataset.

shown in figure 12(a). The increase of n_e^{sep}/n_e^{ped} is correlated with a strong reduction in $\nabla n_e/n_e$. This can be observed both for the datasets at constant β_N (circles and triangles) and for the extended low- δ dataset (squares). The reduction in $\nabla n_e/n_e$ is approximately one order of magnitude. The correlation between n_e^{sep}/n_e^{ped} and η_e is shown in figure 12(b). Both the datasets at constant β_N and the extended low- δ dataset show a positive correlation. Note that η_e depends also on $\nabla T_e/T_e$, so the positive correlation of figure 12(b) is not trivial.

Another interesting observation from figure 12 is that the JET-C subsets tend to have higher $\nabla n_e/n_e$ and lower η_e than the JET-ILW subsets.

7.2. Turbulent transport simulations

Given the correlations shown in figure 12, it is reasonable to suppose that the turbulent transport may play an important role in explaining the pedestal behaviour at high $n_e^{\text{sep}}/n_e^{\text{ped}}$. This hypothesis is investigated using the gyrokinetic code GENE [53]. Of course, also $\nabla T_e/T_e$ will affect the turbulent transport, as suggested for JET-ILW in [27]. However, the present work will focus only on $\nabla n_e/n_e$. A detailed study of the $\nabla T_e/T_e$ effect on the turbulent transport in JET-ILW will be presented in reference [85]. From an experimental point of view, $\nabla T_e/T_e$ has been discussed recently in reference [86]. A further discussion on $\nabla T_e/T_e$ is presented in section 10.1.

The modelling has started from the JET-ILW reference pulse #96202 (low gas, $\beta_N = 1.5$, $n_e^{\text{sep}}/n_e^{\text{ped}} \approx 0.4$). Then, from the reference pulse, the density has been shifted radially inwards and outwards, to mimic the change in $n_e^{\text{sep}}/n_e^{\text{ped}}$, see figure 13(a), with the equilibrium self-consistently recalculated and with the other input parameters kept constant. The shift in the n_e^{pos} leads to a significant variation of the density gradient scale length at the separatrix (and at any other fixed position outside $\psi_N = 0.98$). From a quantitative point of view, the $\nabla n_e/n_e$ values at $\psi_N = 1$ are reported in figure 13(a). $\nabla n_e/n_e$ decreases from $\nabla n_e/n_e \approx 82\psi_N^{-1}$ at $n_e^{\text{sep}}/n_e^{\text{ped}} = 0.24$ to $\nabla n_e/n_e \approx 3\psi_N^{-1}$ at $n_e^{\text{sep}}/n_e^{\text{ped}} = 0.96$. Since the temperature profile is changed only minutely in the present GENE self-consistent the simulations, the reduction of $\nabla n_e/n_e$ with increasing $n_e^{\text{sep}}/n_e^{\text{ped}}$ results in the increase in η_e . These four parameters (n_e^{pos} , $n_e^{\text{sep}}/n_e^{\text{ped}}$, $\nabla n_e/n_e$ and η_e) are strongly correlated among themselves.

The increase of η_e with decreasing $\nabla n_e/n_e$ (via increasing $n_e^{\text{sep}}/n_e^{\text{ped}}$) has a destabilizing effect on slab-ETG micro-instability. This has been determined with linear local GENE simulations. The simulations are fully electro-magnetic, include collisions and parallel magnetic fluctuations and have been done for a range of ballooning angles. No $E \times B$ flow shear has been included and $T_i = T_e$ has been assumed. Slab and toroidal ETG modes have been identified as the dominant micro-instabilities in JET pedestals across a huge range of perpendicular wavenumbers, with slab ETG having the highest growth rates [87]. Therefore, in the following discussion we restrict our attention to slab-ETG micro-instability only. As the slab-ETG mode is relatively insensitive to equilibrium flow shear and details of the T_i profile, the assumptions stated above are not expected to modify the results qualitatively. Moreover, the linear local simulations are suitable for the electron scale and there was no attempt to capture the ion scale. A detailed discussion on the type of modes identified will be presented in reference [85], here we state that slab-ETG modes have been observed. The local linear simulations have been performed at $\rho_{\text{tor}} = 0.97$, $\rho_{\text{tor}} = 0.98$, and $\rho_{\text{tor}} = 0.99$, showing qualitatively similar results among themselves. The linear growth rates at $\rho_{\text{tor}} = 0.98$ are shown in figure 13(b). The increase of $n_e^{\text{sep}}/n_e^{\text{ped}}$ is correlated with the increase in the

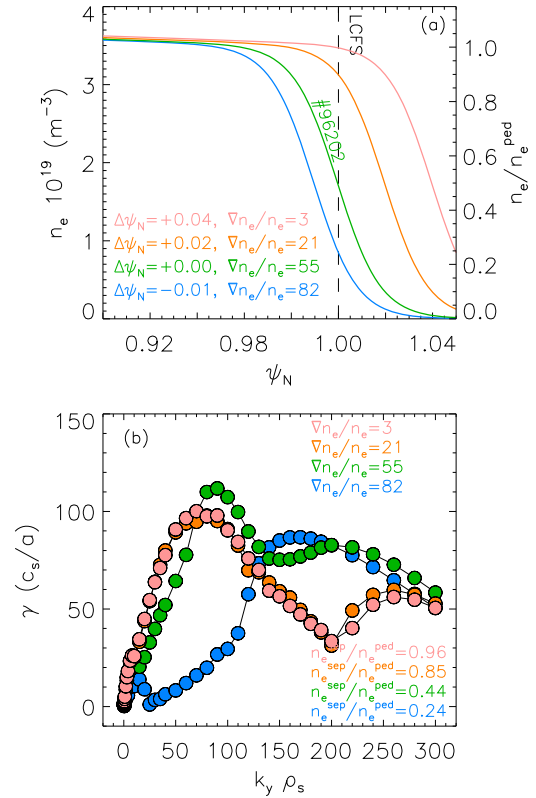


Figure 13. (a) Density profiles used in the GENE simulations. The green line corresponds to the n_e profile of the reference pulse #96202. The other three profiles have been obtained by radially shifting the reference. (b) Corresponding linear growth rates of micro-instabilities at $\rho_{\text{tor}} = 0.98$. The arrow highlight the direction of increasing $n_e^{\text{sep}}/n_e^{\text{ped}}$ and decreasing $\nabla n_e/n_e$.

growth rates, especially in the range $k_y \rho_s = 10$ –100. In particular, the growth rate increase significantly from $n_e^{\text{sep}}/n_e^{\text{ped}} = 0.24$ (a value comparable to JET-C) to $n_e^{\text{sep}}/n_e^{\text{ped}} > 0.44$ (values comparable to JET-ILW plasmas). The result suggests that increasing $n_e^{\text{sep}}/n_e^{\text{ped}}$, along with decreasing $\nabla n_e/n_e$, may lead to increased turbulent transport.

The turbulent transport has been investigated with local non-linear GENE simulations at $\rho_{\text{tor}} = 0.98$. A total of four nonlinear flux-tube slab-ETG simulations were carried out. We used 240, 36, 9 grid points in the z, v_{\parallel}, μ coordinates, with a radial wavenumber grid consisting of 108 cells spanning $k_x \rho_s = 1.28$ to 69.30, and 128 poloidal modes spanning $2.5 \leq k_y \leq 317.5$ corresponding to the slab-ETG range of wavenumbers. Kinetic ions were included in the simulation whilst dynamic impurities were neglected and instead included in the simulations at the level of $Z_{\text{eff}} = 1.8$ (as experimentally estimated). So, the impurities are only represented in the simulation via (i) modifications to the bulk ion density profile, and via (ii) the Z_{eff} term in the collision operator.

The simulated electron heat flux Q_e is shown in figure 14 with full stars and the corresponding electron heat diffusivity χ_e with triangles. For comparison, the experimental P_{sep} has been estimated in the range 3–5 MW at $n_e^{\text{sep}}/n_e^{\text{ped}} \approx 0.2$ and 7–9 MW at $n_e^{\text{sep}}/n_e^{\text{ped}} \approx 0.7$. The total neo-classical heat flux (electron plus ions) determined using NEO [88] is shown

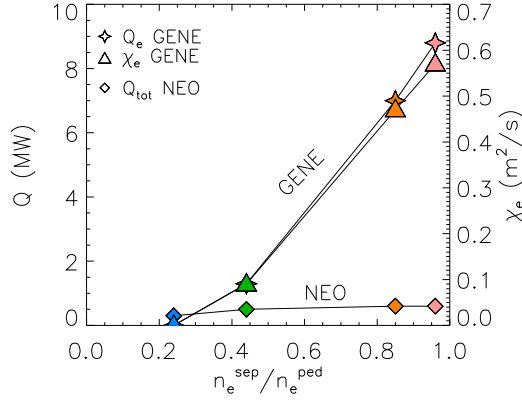


Figure 14. Electron heat flux determined with GENE at $\rho_{\text{tor}} = 0.98$ using the density profiles of figure 13(a) and the input parameters of the JET-ILW reference pulse #96202 (stars). The triangles show the corresponding electron heat diffusivity. The diamonds show the total neo-classical heat flux determined with NEO.

as well. The neo-classical heat flux does not show any strong correlation with $n_e^{\text{sep}}/n_e^{\text{ped}}$. Instead, the slab-ETG turbulent heat flux strongly increases with increasing $n_e^{\text{sep}}/n_e^{\text{ped}}$, from $Q_e \approx 0$ MW at $n_e^{\text{sep}}/n_e^{\text{ped}} \approx 0.2$ up to $Q_e \approx 8$ MW at $n_e^{\text{sep}}/n_e^{\text{ped}} \approx 0.8$ –0.9. It is interesting to observe that the range of $n_e^{\text{sep}}/n_e^{\text{ped}}$ where the slab-ETG turbulent heat flux is low corresponds to the JET-C range ($n_e^{\text{sep}}/n_e^{\text{ped}} < 0.4$).

7.3. Correlation between turbulent transport and experimental pressure gradient

The high level of slab-ETG turbulent heat transport at high $n_e^{\text{sep}}/n_e^{\text{ped}}$ could be the reason for the very low experimental pressure gradients observed at $n_e^{\text{sep}}/n_e^{\text{ped}} > 0.4$. If this hypothesis is correct, we should expect a strong correlation of $\nabla n_e/n_e$ at $\psi_N = 1$ with both the experimental pressure gradient and experimental temperature gradient in the pedestal. This is discussed in figure 15. For reference, figure 15(a) shows the slab-ETG turbulent heat flux versus $\nabla n_e/n_e$ at $\psi_N = 1$. The turbulent transport is clearly higher at low $\nabla n_e/n_e$ than at high $\nabla n_e/n_e$. Figures 15(b) and (c) show the experimental maximum pressure and temperature gradients (respectively) versus $\nabla n_e/n_e$. The pressure gradient has a clear positive correlation with $\nabla n_e/n_e$. Note that $\nabla n_e/n_e$ is determined at the separatrix while ∇p_e corresponds to the maximum gradient, so this correlation is not trivial. By comparing figures 15(b) with figure 15(a), we can observe that the pedestals with the lowest ∇p_e are in the $\nabla n_e/n_e$ range corresponding to the highest turbulent heat flux. The temperature gradients have a similar correlation, however a systematic difference is present between the dataset at constant β_N . This is reasonable since the pulses with higher β_N have more input power.

Figure 15 shows that the experimental data are consistent with the hypothesis that the low pedestal gradients at high $n_e^{\text{sep}}/n_e^{\text{ped}}$ are linked to the increased turbulent transport.

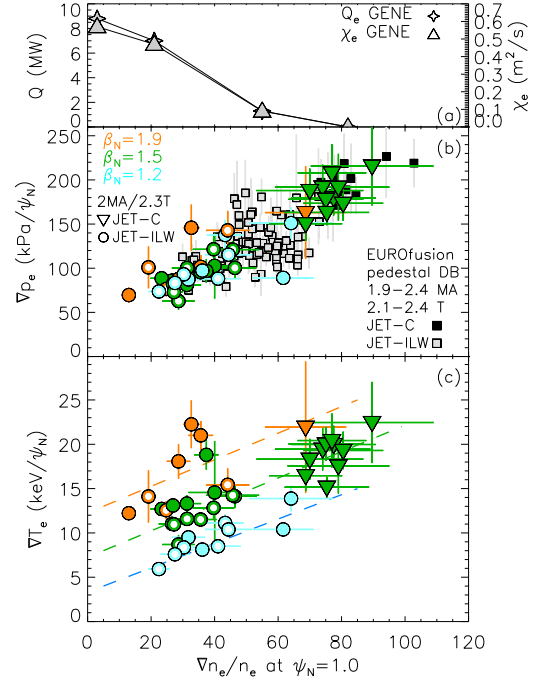


Figure 15. Correlation of (a) turbulent heat flux (b) maximum pressure gradient and (c) maximum temperature gradient with $\nabla n_e/n_e$ determined at $\psi_N = 1$.

8. Empirical links between the increased transport with pedestal width and with MHD stability

Section 6 has identified two issues related to the disagreement between the Europed pedestal predictions and the experimental results at $n_e^{\text{sep}}/n_e^{\text{ped}} > 0.4$. The first is the related to the incorrect predictions of the pedestal width, figure 10, the second to the fact that the pre-ELM pedestal tends not to reach the ideal MHD PB boundary, figure 11. In section 7, we have shown that the increase of $n_e^{\text{sep}}/n_e^{\text{ped}}$ can lead to a significant increase of the turbulent transport. This section discusses some empirical links that try to connect the increased transport with the wider width and with the disagreement with ideal MHD.

8.1. Possible link between turbulent transport and pedestal width

In JET-ILW, a scaling of the pedestal pressure width using a large database has been very challenging to identify. At low gas rate, the pedestal width follows reasonably well the EPED1 model (see for example [15, 24, 27]), while the deviation from EPED1 increases significantly with increasing gas rate [24, 27, 89]. So far, the attempts to identify a multi-variable scaling of the pedestal width in JET have been unsuccessful [24]. However, $\nabla n_e/n_e$ was one of the variables that were not tested in any JET multi-variable scaling.

Figure 16(a) shows the pedestal pressure width versus $\nabla n_e/n_e$ at $\psi_N = 1$. The negative correlation is remarkable. This is the first time in JET that a clear scaling of the pedestal width is observed using datasets with different gas rate and power.

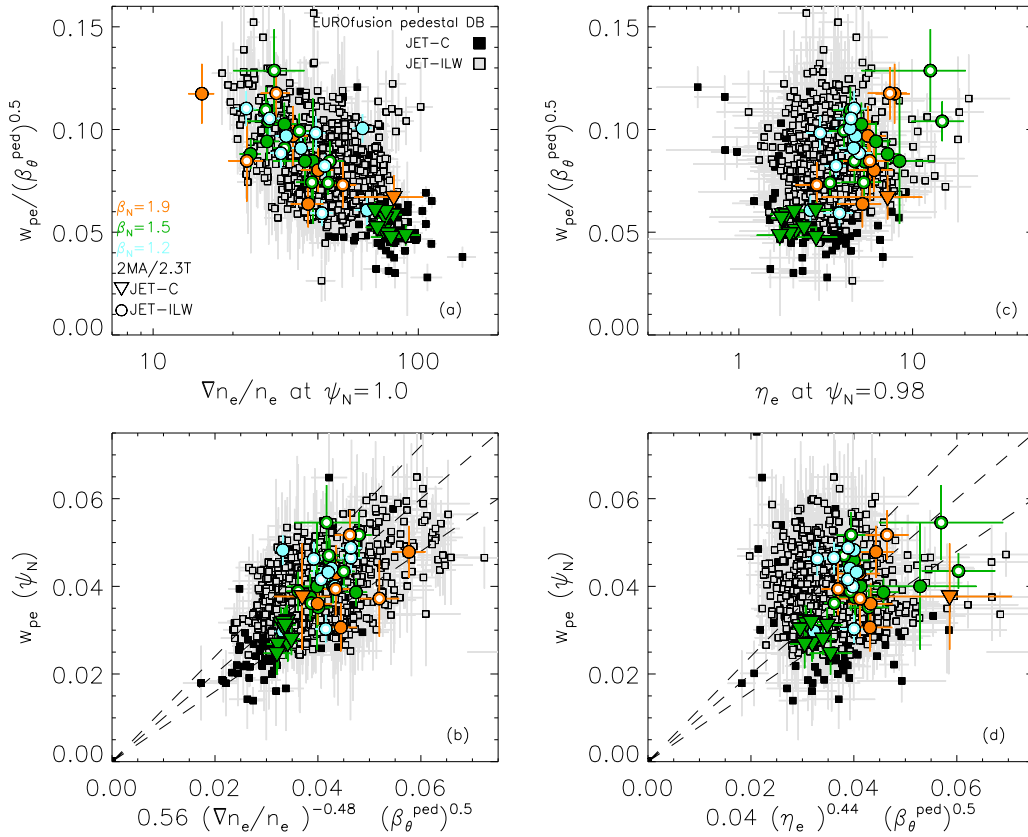


Figure 16. (a) Correlation between the experimental pressure width w_{pe} normalized to $(\beta_{\theta}^{ped})^{0.5}$ and $\nabla n_e/n_e$ at the separatrix. (b) Comparison between w_{pe} and the scaling law proposed in expression (3). (c) Correlation between $w_{pe}/(\beta_{\theta}^{ped})^{0.5}$ and η_e . (d) Comparison between $w_{pe}/(\beta_{\theta}^{ped})^{0.5}$ and a power law fit using η_e . The dashed lines highlight the perfect agreement and a $\pm 20\%$ variation.

Moreover, the JET-C widths are reasonably well aligned with the JET-ILW widths. We should note that the use of η_e , instead of $\nabla n_e/n_e$, still produces a reasonable trend when considering the constant β_N datasets. However, when using the extended low- δ dataset no clear correlation between width and η_e can be observed, see figure 16(c). This could be due to the fact that a reliable estimation of η_e over a large dataset is challenging (being the ratio of two gradients, the uncertainty can be very large). Note that in figure 16(c) the parameter η_e has been determined at the radial position that gives the best correlation ($\psi_N = 0.98$). An even poorer correlation for the extended low- δ dataset has been obtained at $\psi_N = 1.0$.

Given the empirical correlation of figure 16(a), the following hypothesis can be put forward to explain the correlation between w_{pe} and $\nabla n_e/n_e$ in the constant β_N datasets. The increase of the gas rate produces the increase of n_e^{sep}/n_e^{ped} (see section 5), which leads to the reduction of $\nabla n_e/n_e$ (see figure 12) and to the increases of the pedestal turbulent transport (see section 7). However, the datasets are composed of pulses with constant β_N , so more power is necessary at low $\nabla n_e/n_e$ to keep β_N constant. Since at low $\nabla n_e/n_e$ the pressure gradient is limited by the high turbulent transport, figure 15(a), the increase of the power can lead to the increase of the pedestal height only via the pedestal width widening. This chain of events could explain the negative correlation between pedestal width and $\nabla n_e/n_e$ shown in figure 6(a). However, more specific studies are necessary to fully test this idea.

In terms of multi-variable scaling, it is important to remember that the JET-ILW width is in agreement with EPED1 at low gas rate [15, 24] and that the EPED1 width scaling works reasonably well in other machines like Alcator C-Mod [90], AUG [91], DIII-D [47, 92] and JT-60U [93–95]. We therefore propose the following modification as a generalization of the EPED1 scaling:

$$w_{pe} = k \left(\frac{\nabla n_e}{n_e} \right)^{\alpha} \left(\beta_{\theta}^{ped} \right)^{0.5}, \quad (3)$$

where the $\nabla n_e/n_e$ terms represents the slab-ETG turbulent transport effect. In expression (3), both gradients are done in normalized poloidal flux units ψ_N and the width is expressed in ψ_N . This scaling is tested in figure 16(b), using $k = 0.56$ and $\alpha = -0.48$ (determined from a power law fit). The correlation is very good for the datasets at constant β_N . The correlation is still reasonable but not perfect for the extended low- δ dataset. It is however a significant improvement from any other width scaling obtained in JET, so far. This has been quantified by calculating the correlation coefficients for the extended low- δ dataset. The correlation coefficient between the experimental w_{pe} and the standard EPED1 scaling of expression (2), see figure 10(c), is $R^2 = 0.03$. The correlation coefficient between w_{pe} and the improved scaling of expression (3) is $R^2 = 0.65$. It is interesting to note that at low gas rate or for the JET-C dataset, $\nabla n_e/n_e$ is in the range $(50-100)\psi_N^{-1}$. For these values,

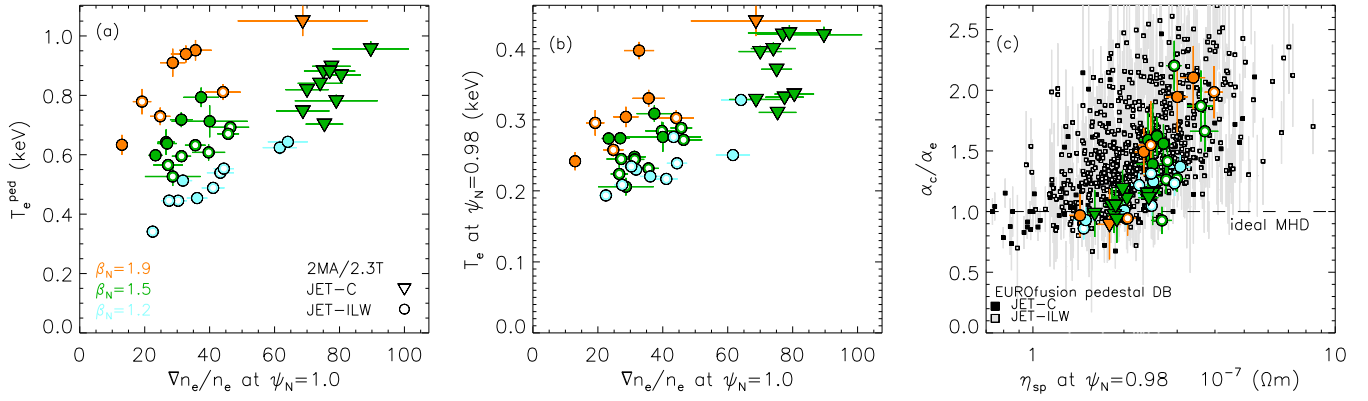


Figure 17. Correlation of (a) electron temperature at the pedestal top and (b) in the middle of the pedestal (at $\psi_N = 0.98$) with $\nabla n_e/n_e$ determined at the separatrix. (c) Correlation between $\alpha_{\text{crit}}/\alpha_{\text{exp}}$ and the Spitzer resistivity (determined at $\psi_N = 0.98$).

the term $0.56(\nabla n_e/n_e)^{-0.48}$ is in the range 0.061–0.085, which is consistent with the standard EPED1 coefficient, 0.076. This suggests that the improved width scaling of expression (3) might be valid also in other machines, where the standard EPED1 scaling produces reasonable width predictions. In fact, most of the other machines tends to operate at low $n_e^{\text{sep}}/n_e^{\text{ped}}$ in type I ELMy H-modes (see section 10.3 for a more extended discussion).

For completeness, figure 16(d) tests the scaling law $w_{pe} = k\eta_e^\alpha (\beta_\theta^{\text{ped}})^{0.5}$. The scaling law is rather poor using the extended low- δ dataset ($R^2 = 0.05$), but it is more reasonable when using the constant β_N datasets ($R^2 = 0.65$). As mentioned above, this could be due the fact that the η_e estimation is challenging over a large dataset, but it could also suggest that the physics that determines the pedestal width is more related to $\nabla n_e/n_e$ than to η_e . For reference, the coefficients determined using the constant β_N datasets are $k = 0.04$ and $\alpha = 0.44$.

8.2. Possible link between turbulent transport and the disagreement with ideal MHD stability

Figure 11(b) has shown that a large part of the dataset is not in agreement with the ideal MHD PB stability at high $n_e^{\text{sep}}/n_e^{\text{ped}}$. This section discusses a possible link between the increased transport at high $n_e^{\text{sep}}/n_e^{\text{ped}}$ and the disagreement with ideal MHD. The discussion will lead to the hypothesis that resistive MHD might be necessary to describe the ELM triggering mechanism at high $n_e^{\text{sep}}/n_e^{\text{ped}}$.

As discussed in section 7, the increase of $n_e^{\text{sep}}/n_e^{\text{ped}}$ leads to the increase of the turbulent transport, which is correlated with the reduction of the pedestal gradients (see figure 15). This suggests that the increase of $n_e^{\text{sep}}/n_e^{\text{ped}}$ (and the reduction of $\nabla n_e/n_e$) should be correlated with the reduction of the temperature in the pedestal region. Indeed, the experimental results shown in figures 17(a) and (b) support this conclusion. Figure 17(a) shows the correlation between the temperature at the pedestal top (T_e^{ped}) versus $\nabla n_e/n_e$. Figure 17(b) shows the correlation between the temperature determined in the middle of the pedestal region (for simplicity a fixed position at $\psi_N = 0.98$ has been chosen) versus $\nabla n_e/n_e$. In both cases, the reduction of $\nabla n_e/n_e$ is correlated with the reduction of the

temperature. Of course, a systematic difference between the subsets with different β_N is present. This is because the temperature tends to increase with increasing β_N .

Due to the lower temperature, pedestals at high $n_e^{\text{sep}}/n_e^{\text{ped}}$ will also have high resistivity. Figure 17(c) shows the correlation between $\alpha_{\text{crit}}/\alpha_{\text{exp}}$ and the Spitzer resistivity η_{sp} determined in the middle of the pedestal, at $\psi_N = 0.98$ (with $\eta_{\text{sp}} = 1.65 \times 10^{-9} Z_{\text{eff}} \ln \Lambda T_e^{-3/2}$). The datasets at constant β_N show a rather clear correlation. Pedestals that do not reach the ideal MHD stability boundary tend to have resistivity higher than those limited by ideal MHD. Note that the JET-C dataset is near the ideal MHD boundary and is characterized by low resistivity. Figure 17(c) shows also the correlation for the extended low- δ dataset. The scatter is rather large, but a positive correlation is present. The large scatter could be due to the fact figure 17(c) correlates a dimensionless parameter ($\alpha_{\text{crit}}/\alpha_{\text{exp}}$) with a dimensional parameter (η_{sp}). Unfortunately, a reasonable normalization for η_{sp} has not been found yet.

Figure 17(c) suggests that resistive MHD might be necessary to correctly describe the pedestal stability at high $n_e^{\text{sep}}/n_e^{\text{ped}}$. Similar hypothesis were put forward also in references [41, 96].

9. Initial results on the effect of resistive MHD on pedestal stability

The linear resistive MHD stability code CASTOR [44] has been used to test the hypothesis that resistive MHD might be necessary at high $n_e^{\text{sep}}/n_e^{\text{ped}}$ to explain the ELM triggering mechanism. This investigation is still in its initial stages and the aim of the section is only to show a proof principle, i.e. that resistive MHD might be helpful to move the PB stability boundary closer to the experimental point and to reconcile the JET-ILW results at high $n_e^{\text{sep}}/n_e^{\text{ped}}$ with the theoretical description of the ELMs.

As discussed in section 3.2, the same workflow used for ideal PB stability is used, with j_{bs} determined with the Sauter formula and the equilibrium determined with HELENA. The same stability criterion used for the ideal MHD ($\gamma = 0.03\omega_A$) has been applied. For simplicity, a flat resistivity profile is used. The modelling has been done for the JET-ILW reference pulse

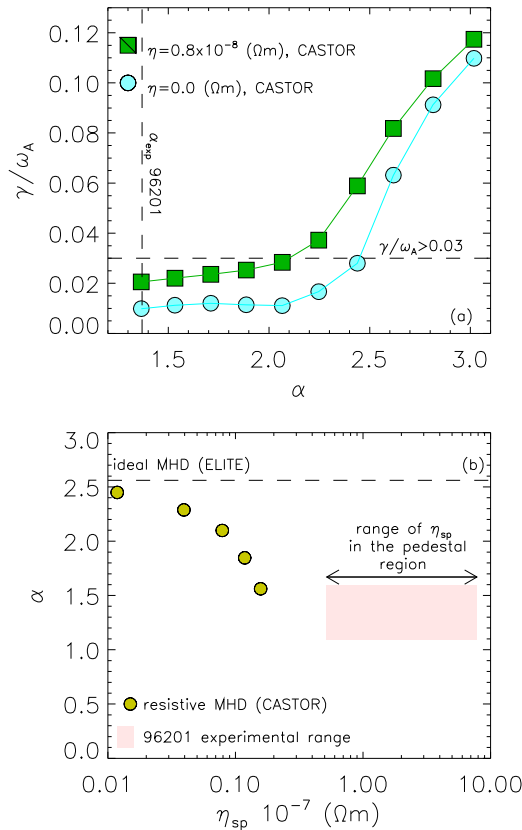


Figure 18. (a) Dependence of the growth rate of the most unstable mode determined with CASTOR with the normalized pressure α . The vertical line shows α_{exp} of the reference pulse and the horizontal line the stability threshold. The circles show the ideal case and the squares the case with $\eta = 0.8 \times 10^{-8} \text{ } \Omega\text{m}$. (b) Dependence of α_{crit} with resistivity. The circles highlight CASTOR results while the horizontal dashed line the ideal MHD results with ELITE. The red shaded area highlights the experimental range in the pedestal region of the reference pulse #96201.

#96201 (high gas rate, $\beta_N = 1.5$, $n_e^{\text{sep}}/n_e^{\text{ped}} \approx 0.8$, $\alpha_{\text{crit}}/\alpha_{\text{exp}} \approx 1.8$ from ideal MHD). The corresponding ideal MHD PB stability boundary is shown in figure 5 (dark yellow data).

Figure 18(a) shows the dependence of growth rate of the most unstable mode predicted by CASTOR with the normalized pressure gradient α . The results are obtained by determining the growth rates of the modes in the range $n = 5\text{--}70$ starting from the pre-ELM experimental profiles ($\alpha \approx 1.4$). The modelling is then repeated by increasing the temperature and self-consistently re-calculating j_{bs} , equilibrium and stability. Figure 18(a) shows with light blue circles the CASTOR results for the ideal case. The stability threshold ($\gamma = 0.03\omega_A$) is exceeded at $\alpha_{\text{crit}} \approx 2.5$, in agreement with the results obtained with ELITE and shown in figure 5. The most unstable modes are in the range $n = 50\text{--}70$, consistent with what determined with ELITE and consistent with a ballooning instability. The CASTOR results using a non-zero flat resistivity profile ($\eta = 0.8 \times 10^{-8} \text{ } \Omega\text{m}$) are shown in figure 18(a) with green squares. The increase of the resistivity tends to increase the growth rates and the stability threshold is exceeded at $\alpha_{\text{crit}} \approx 2.1$, a value lower than in the ideal case. The most unstable

modes are still in the range $n = 50\text{--}70$, so still consistent with a ballooning instability.

The results of a resistivity scan are presented in figure 18(b), where α_{crit} versus resistivity is shown. The red shaded area highlights the experimental range of #96201, while the horizontal dashed line shows the result from ideal MHD obtained with ELITE. CASTOR results are consistent with ideal MHD at low resistivity. In particular, for very low resistivity ($\eta < 0.02 \times 10^{-7} \text{ } \Omega\text{m}$) resistive MHD and ideal MHD produces very similar result. Above $\eta \approx 0.02 \times 10^{-7} \text{ } \Omega\text{m}$, the increase of resistivity reduces significantly α_{crit} . Unfortunately, the agreement with the experimental results is not good yet. The predicted α_{crit} is reduced to values comparable to α_{exp} for a resistivity approximately a factor 5 lower than the experimental one. The disagreement might be due to several reasons, for example the use of a flat resistivity profile in the modelling or the fact the modes destabilized at high resistivity might not be able to trigger ELMs.

While further investigation is still ongoing and no conclusive claims are possible, this section shows that the inclusion of resistivity in the MHD stability analysis has the potential to address the problem of the ELM triggering mechanisms at high $n_e^{\text{sep}}/n_e^{\text{ped}}$.

10. Discussion

The work has shown that the separatrix density, more precisely the ratio $n_e^{\text{sep}}/n_e^{\text{ped}}$, has a significant effect on the pedestal height. This effect has been fully understood at low $n_e^{\text{sep}}/n_e^{\text{ped}}$, where it is due to the impact of pressure profile position on ideal PB stability, while at high $n_e^{\text{sep}}/n_e^{\text{ped}}$ the increase turbulent transport requires higher power to reach the same pedestal high and resistive MHD may be required to explain the instability causing the ELM. This section (1) discusses the issues that are still open, (2) compares the earlier conclusions on $\alpha_{\text{crit}}/\alpha_{\text{exp}} > 1$ with the present results, (3) discusses the link between the present results and the results in other machines including comments related to ITER and (4) proposes a possible workflow to improve the pedestal predictions in JET.

10.1. Open issues

The work has discussed several physics mechanisms to explain the pedestal degradation with increasing $n_e^{\text{sep}}/n_e^{\text{ped}}$. In some cases, the modelling of these mechanisms has produced only a qualitative agreement, while in other cases several effects have been neglected for simplicity. This subsection summarizes all the open issues and the work that is planned for the near future.

10.1.1. Scrape-off layer. In section 5, the modelling of the behaviour of $n_e^{\text{sep}}/n_e^{\text{ped}}$ and n_e^{pos} with the gas rate has produced a reasonable qualitative agreement with the experimental data. The increase of the gas rate has led to an increase in $n_e^{\text{sep}}/n_e^{\text{ped}}$ and n_e^{pos} both in the experiment and in the JIN-TRAC results. While this modelling has revealed insights in the mechanisms that regulates $n_e^{\text{sep}}/n_e^{\text{ped}}$ and n_e^{pos} , it is not yet predictive.

The modelling has assumed no change in the transport coefficients with increasing gas rate. The increasing gas rate leads to an increase in $n_e^{\text{sep}}/n_e^{\text{ped}}$ which, according to the results discussed in section 7, should increase the heat transport coefficient (we might also anticipate changes in the particle transport). A first principles based model for plasma transport is needed to replace prescribed transport coefficients, if we are to make predictive simulations of the pedestal profiles. This is unfortunately not yet possible.

No attempt has yet been made to compare the experimental and modelled divertor and SOL characteristics. This type of work requires a specific effort. However, initial results have been presented in [61] and will be further investigated in [62] using a dataset consistent with the plasmas used in the present work (same I_p , same B_t , same plasma shape and comparable power and gas ranges), where the correlations between n_e^{sep} with the SOL and the target conditions will be discussed.

10.1.2. Turbulent transport modelling and role of $\nabla T_e/T_e$. The turbulent transport modelling discussed in section 7 has been devoted only to investigate the effect of $\nabla n_e/n_e$, as this is a parameter directly related with $n_e^{\text{sep}}/n_e^{\text{ped}}$. Of course, also $\nabla T_e/T_e$ will also play a significant role via η_e . This is now under investigation with GENE and novel results on the role of $\nabla T_e/T_e$ in JET-ILW gas and power scans will be reported soon [85]. From an experimental point of view, $\nabla T_e/T_e$ has been discussed recently in reference [86], where it was shown from JET-ILW power and gas scans that the pedestal heat transport is in general not particularly stiff, i.e. that η_e is not strongly clamped to the expected linear threshold for ETG turbulence. Moreover, the dependence of T_e^{ped} on $n_e^{\text{sep}}/n_e^{\text{ped}}$ is currently under investigation to test a heuristic model based on stiff ETG turbulent heat transport and results are to be reported in a future publication [97].

The turbulent transport modelling has not attempted to capture the ion scale, but we might expect slab-ITG more linearly stable than slab-ETG. As discussed in section 3, for the plasmas used in this work T_i^{ped} is equal to T_e^{ped} from the core to the pedestal top, while $T_i^{\text{sep}} > T_e^{\text{sep}}$ can be expected. This implies $\nabla T_i/T_i < \nabla T_e/T_e$ in the pedestal and hence $\eta_i < \eta_e$. Coupled with the increased susceptibility of slab-ITG modes to equilibrium flow shear, we may expect slab-ITG to be more linearly stable than slab-ETG which may be translated into less ion heat transport. However, this cannot be fully excluded yet, as discussed in [75, 98].

10.1.3. Pedestal width. The work has shown that at low $\nabla n_e/n_e$ and high $n_e^{\text{sep}}/n_e^{\text{ped}}$ the slab-ETG driven turbulent transport dominates over the neo-classical transport in the pedestal region. For this reason, an extension of the EPED1 width scaling with a new term dependent on $\nabla n_e/n_e$ has been proposed. The new scaling law, expression (3), reproduces the experimental w_{pe} significantly better than the standard EPED1 expression. However, the coefficients of expression (3) are empirically estimated. At the moment it is unclear if these coefficients can be valid in other machines. Given the large scatter shown in figure 16(a) we cannot even exclude that

further physics parameters, necessary to describe other transport mechanisms, need to be included.

Assuming that the problem related with the MHD stability will be resolved (perhaps using resistive MHD), we could envisage a predictive modelling for w_{pe} similar to EPED1.6 [47]. The resistive stability boundary would give the first constraint to link the pedestal height to w_{pe} . Then, the turbulent transport modelling (ideally based on a reduced model) would give the second constraint to link the pedestal height to w_{pe} . The intersection of the two constraints would identify the predicted height and width. The challenging part in this approach will be to develop a reduced transport model general enough to include both slab-ETG and KBM transport.

10.1.4. Role of resistivity. Section 9 has shown that resistive MHD might help to explain the ELM triggering mechanism at high $n_e^{\text{sep}}/n_e^{\text{ped}}$. This investigation is still in its initial stages and at the moment it is unclear if resistive MHD can fully solve the problem. The topic is under investigation and in the medium term a conclusive answer will be available. Moreover, we cannot exclude that other effects might contribute to explain the ELM triggering mechanism. For example, the plasma viscosity could also play a role, with a stabilizing effect on the ballooning modes [96, 99, 100]. The diamagnetic term and plasma rotation can also contribute [41, 42].

It is also worth to notice that the resistivity can be high not only due to a low of T_e^{ped} . Also a wide pedestal can lead to low resistivity. This is because the separatrix temperature is typically rather constant (around 100 eV in JET). So, the temperature at a fixed radial position can decrease also due to the widening of the pedestal. This has been tested by modelling the temperature profile with the mtanh function and determining the temperature at $\psi_N = 0.98$. Figure 19(a) shows an example using $T_e^{\text{ped}} = 0.8$ keV for a very narrow pedestal ($w_{pe} = 0.025\psi_N$) and a very wide pedestal ($w_{pe} = 0.07\psi_N$). The resistivity profiles have been determined assuming $Z_{\text{eff}} = 1$ and are shown in figure 19(b). The resistivity at fixed location inside the separatrix is clearly higher for the wider pedestal profile. For example, at $\psi_N = 0.98$ the difference is approximately one order of magnitude. Note that the uncertainty on T_e^{sep} does not affect significantly this conclusion. This can be seen from the shaded areas in figures 19(a) and (b) which show the effect of a 20% variation in T_e^{sep} , in the range 80–120 eV. This approach has been repeated using different pedestal width and pedestal height and assuming $T_e^{\text{ped}} = 100$ eV. The results are summarized in figure 19(c), where the datasets at constant β_N are also shown for reference. At constant T_e^{ped} the resistivity at $\psi_N = 0.98$ can increase significantly. In principle, it is possible to have pedestals with $T_e^{\text{ped}} = 1.0$ keV but with resistivity at $\psi_N = 0.98$ comparable to pedestals with $T_e^{\text{ped}} = 0.3$ keV. These observations suggest that resistive MHD might be relevant also in high temperature pedestals. For example, this could be important for the new zero gas regime recently obtained in JET-ILW [101, 102]. This regime has a relatively high electron pedestal temperature ($T_e^{\text{ped}} \approx 1$ keV), a large pedestal width ($w_{pe} \approx 0.06$ – $0.07\psi_N$) and a pedestal not limited by ideal MHD [102]. This regime

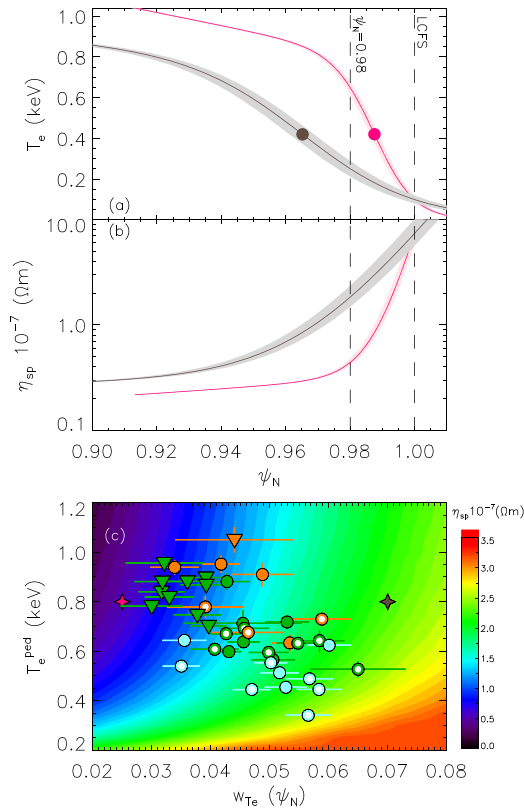


Figure 19. (a) Example of T_e profiles with same T_e^{ped} and $T_e^{\text{sep}} = 100$ eV but different width. The dots identify the position of the maximum gradient. The shaded areas highlight the effect on the profiles of a variation in T_e^{sep} in range 80–120 eV. (b) Corresponding Spitzer resistivity profiles assuming $Z_{\text{eff}} = 1$. (c) Dependence of Spitzer resistivity at $\psi_N = 0.98$ with pedestal temperature width and height. A mtanh function has been assumed to describe the T_e profile. The circles and the triangles represent the constant β_N datasets with same colour and symbol definitions as in the previous figures. The stars highlight the position of the profiles used in frame (a).

is located in the top right of figure 19(c), where the resistivity is rather high and comparable to the low T_e^{ped} data of the constant β_N dataset. So we could speculate that resistive MHD might be important to explain the ELM mechanisms also in the new JET-ILW zero gas regime. We should note that the zero gas regime is characterized by small ELMs, and not by type I ELMs. So it is equally possible that a further new mechanism must be invoked for the zero gas regime.

10.1.5. Pedestal performance in JET-ILW versus JET-C. This work has shown that JET-C pedestals tend to be characterized by lower $n_e^{\text{sep}}/n_e^{\text{ped}}$, lower η_e and higher $\nabla n_e/n_e$ than JET-ILW plasmas. This is likely due to the different fuelling rate typical in the two machines, which was typically very low in JET-C while for operational reasons is higher in JET-ILW. This difference can explain, at least in part, the lower pedestal confinement in JET-ILW. From one side, the high $n_e^{\text{sep}}/n_e^{\text{ped}}$ typical of JET-ILW leads to high pedestal transport (via the low $\nabla n_e/n_e$ and the high η_e) and to $\alpha_{\text{crit}}/\alpha_{\text{exp}} > 1$. From the other side, the low $n_e^{\text{sep}}/n_e^{\text{ped}}$ typical of JET-C leads to low turbulent

transport and to density profiles located radially more inwards than in JET-ILW, improving the PB stability. The Europed modelling shown in figure 6(b) indeed shows that the change in the PB stability due to the change in n_e^{pos} can reproduce the experimental JET-C trend.

However, very likely this is not the only reason that explains the difference between JET-C and JET-ILW. For example, low-Z impurities play an important role too. Seeding of low-Z impurities in metal wall machines tends to increase the pedestal pressure as observed in several machines [6–8, 11, 12, 103]. So it is likely that the lack of intrinsic C impurities in JET-ILW can contribute as well to explain the difference in the pedestal pressure between JET-C and JET-ILW.

10.2. Comparison with earlier JET-ILW results on the discrepancy between ideal MHD and ELM mechanism

Several earlier works have presented experimental results on the disagreement between the ideal PB stability and the ELM triggering mechanism in JET-ILW type I ELMy H-modes [3, 15, 18, 24, 27, 28]. The key earlier results are that $\alpha_{\text{crit}}/\alpha_{\text{exp}} \gg 1$ occurs at high power and high gas rate (in terms of engineering parameters) [15] and at high relative shift, $n_e^{\text{pos}} - T_e^{\text{pos}}$ (in terms of plasma parameters) [24]. These results were shown to be consistent with each other since $n_e^{\text{pos}} - T_e^{\text{ped}}$ increases both with increasing gas rate and with increasing power [24].

The results of the present work are consistent with these earlier conclusions. First of all, figure 20(a) shows the correlation between $\alpha_{\text{crit}}/\alpha_{\text{exp}}$ and the relative shift for the constant β_N datasets. The JET-ILW subsets have the same positive correlation already observed in [24]. This is because the relative shift is strongly correlated with $n_e^{\text{sep}}/n_e^{\text{ped}}$, as shown in figure 20(b). The increasing $n_e^{\text{sep}}/n_e^{\text{ped}}$ leads to an increasing n_e^{pos} and hence to an increasing $n_e^{\text{pos}} - T_e^{\text{pos}}$. Moreover, we can see from figure 20(b) that the highest relative shifts are achieved at the highest power. This is because the increasing power and the high gas rate tends to increase the pedestal width and hence to move the temperature profile radially inwards, see the example shown in figure 19(a). A novel result of figure 20(a) is that the positive correlation between $\alpha_{\text{crit}}/\alpha_{\text{exp}}$ and $n_e^{\text{pos}} - T_e^{\text{pos}}$ saturates at very low relative shift. This is particularly clear for the JET-C subset, which has the $n_e^{\text{pos}} - T_e^{\text{pos}} \approx 0.01$, but still $\alpha_{\text{crit}}/\alpha_{\text{exp}} \approx 1$.

Using the results discussed in this work, we can propose a qualitative explanation for the empirical results that $\alpha_{\text{crit}}/\alpha_{\text{exp}} \gg 1$ occurs at high gas and high power [15]. First of all, we should stress that the conclusions discussed in [15] are that the high power in combination with the high gas rate lead to $\alpha_{\text{crit}}/\alpha_{\text{exp}} \gg 1.0$. High power alone or high gas rate alone do not lead to $\alpha_{\text{crit}}/\alpha_{\text{exp}} \gg 1$. The high gas rate leads to high $n_e^{\text{sep}}/n_e^{\text{ped}}$ and hence to high the slab-ETG transport, which limits the pedestal gradients. In these conditions, the increase of the power might lead only to a very weak increase in the pedestal gradients. The increased power could still widen the pedestal. Being $T_e^{\text{sep}} \approx 100$ eV, the pedestal widening leads a T_e reduction at a fixed position which in turn leads to the increase of resistivity (see figure 19 for an example), possibly making the resistive MHD effects non-negligible anymore. It

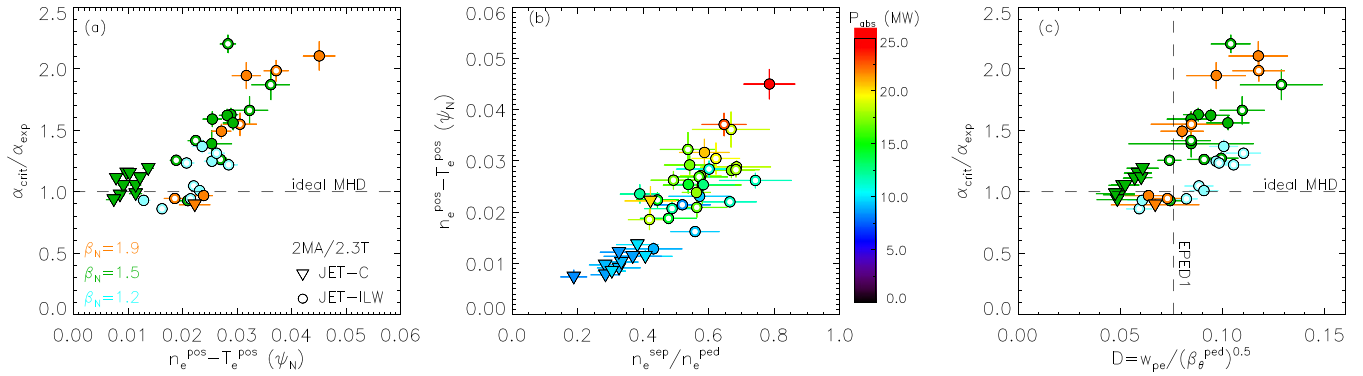


Figure 20. (a) Correlation between $\alpha_{\text{crit}}/\alpha_{\text{exp}}$ with the relative shift. (b) Correlation between the relative shift with $n_e^{\text{sep}}/n_e^{\text{ped}}$ and with power. (c) Correlation between $\alpha_{\text{crit}}/\alpha_{\text{exp}}$ with the coefficient D .

is also possible the widening of the pedestal width is due to the fact that the resistive MHD modes do not go unstable until the pedestal is sufficiently broad. At the moment, these are only hypotheses and a conclusive answer can be achieved only after a detailed turbulent transport modelling that assesses the role of both $\nabla n_e/n_e$ and $\nabla T_e/T_e$ and a detailed resistive MHD study. Concerning the role of the power, it is also possible that the increase of the power at high gas rate leads to a further increase in $n_e^{\text{sep}}/n_e^{\text{ped}}$. In fact, in low- δ plasma n_e^{ped} tends to decrease with increasing power (see for example [104]). This would further reduce $\nabla n_e/n_e$ and further increase the pedestal transport.

Another interesting empirical result discussed in reference [24] is that $\alpha_{\text{crit}}/\alpha_{\text{exp}}$ is positively correlated with the coefficient D , defined as $w_{pe} = D(\beta_\theta^{\text{ped}})^{0.5}$ (a generalization of the EPED1 model, which assumes $D = 0.076$). The present constant β_N datasets have the same correlation, as shown in figure 20(c). Now, we are in a position to propose an explanation for this correlation, which in [24] was presented only as an empirical result. The coefficient D in the EPED1.6 is supposed to contain information related to the pedestal transport. In section 8.1, expression (3) and figure 16(a), we have shown that D is strongly correlated with $(\nabla n_e/n_e)^{-0.48}$ hence, likely, with slab-ETG turbulent transport. So, the correlation of figure 20(c) is simply highlighting that $\alpha_{\text{crit}}/\alpha_{\text{exp}} > 1$ occurs at low $\nabla n_e/n_e$ where the turbulent transport is high.

10.3. Comparison with other machines and discussion on possible effect for ITER

Most of the present machines tend to work at relatively low $n_e^{\text{sep}}/n_e^{\text{ped}}$ in type I ELMy H-modes. For example, in AUG a typical range is $n_e^{\text{sep}}/n_e^{\text{ped}} \approx 0.1-0.5$ [11], in TCV $n_e^{\text{sep}}/n_e^{\text{ped}} \approx 0.1-0.4$ [105], in DIII-D $n_e^{\text{sep}}/n_e^{\text{ped}} \approx 0.2-0.6$ [21, 22], in Alcator C-Mod $n_e^{\text{sep}}/n_e^{\text{ped}} \approx 0.1-0.35$ [64, 65]. These are the ranges in JET in which (i) the behaviour of the pedestal pressure can be explained via the outward shift of the density profile and (ii) the EPED1 model produces a reasonable agreement with the experimental data. At low $n_e^{\text{sep}}/n_e^{\text{ped}}$ the ELMs tend to be triggered at the ideal PB boundary and the term $0.56(\nabla n_e/n_e)^{-0.48}$ in expression (3) is reduced to the range 0.061–0.085, which is consistent with the EPED1 assumption

(0.076). The low $n_e^{\text{sep}}/n_e^{\text{ped}}$ could explain why the EPED1 model works reasonably well in most of the machines [106], including JET-C, while in JET-ILW disagreements are often observed [28].

Nonetheless, high $n_e^{\text{sep}}/n_e^{\text{ped}}$ can be achieved in other machines with high gas rate and/or high seeding rate. For example, in Alcator C-Mod $n_e^{\text{sep}}/n_e^{\text{ped}} \approx 0.8$ has been reached with neon and nitrogen seeding [13, 55] and a clear negative correlation of H_{98} , pedestal pressure and pedestal temperature with increasing $n_e^{\text{sep}}/n_e^{\text{ped}}$ have been observed.

At present, it is unclear how these results will affect the pedestal predictions for ITER. ITER is supposed to operate at high $n_e^{\text{sep}}/n_e^{\text{ped}}$ (see, for example, [107–109]) so the present results might have a strong impact on ITER predictions. However, ITER is also supposed to operate at very low collisionality (see for example [47]), likely with the pedestal near the peeling boundary. The present results have been obtained with pedestal closer the ballooning boundary rather than to the peeling, so it is not possible to directly extrapolate the present conclusions to ITER. For example, results discussed in [110] suggests that on the peeling boundary an increase of pedestal pressure with increasing n_e^{sep} can be expected. Further investigation is necessary to achieve conclusive claims on the $n_e^{\text{sep}}/n_e^{\text{ped}}$ effect on ITER predictions.

10.4. Improved pedestal predictions in JET-ILW

If resistive MHD effects will prove to be the key element to explain the ELM triggering mechanism at high $n_e^{\text{sep}}/n_e^{\text{ped}}$, we can propose the following improvement in the Europed modelling. At present, ideal MHD and the KBM transport constraint, expression (2), are sufficient to reach a reasonable pedestal prediction at low $n_e^{\text{sep}}/n_e^{\text{ped}}$. At high $n_e^{\text{sep}}/n_e^{\text{ped}}$, the model overestimates the pedestal pressure height and underestimates the pressure width, as schematically shown in figure 21. To overcome the problem, the following approach is proposed. Since slab-ETG transport is present in the pedestal, the KBM constraint can be updated using a more general model for describing the pedestal width. For example, expression (3) includes both the term $(\beta_\theta^{\text{ped}})^{1/2}$ for the KBM transport and the term $\nabla n_e/n_e$ for the slab-ETG transport. The inclusion of the slab-ETG term would lead to a wider

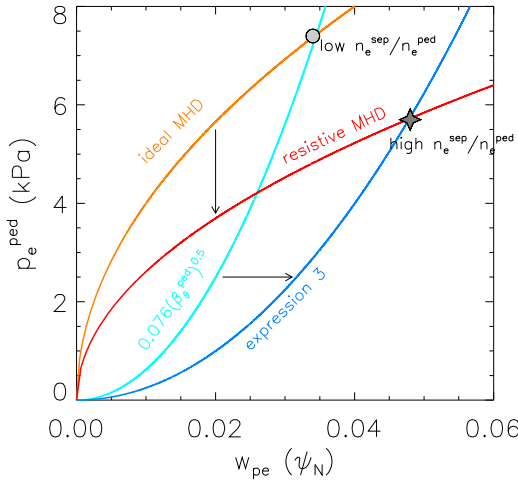


Figure 21. Schematic illustration of the effect of the new transport constraint, expression (3), and of resistive MHD on the pedestal predictions.

pedestal width at high $n_e^{\text{sep}}/n_e^{\text{ped}}$, see figure 20. It is likely that expression (3) is still an oversimplification (depending on plasma parameters other micro-instabilities might be present), it is however a significant improvement from the standard EPED1 approach, as can be concluded by comparing figures 10(c) and 16(b). However, the use of expression (3) would not be sufficient to improve the prediction, as a wider pedestal would lead to a further overestimation of the pedestal height. The second step would be to replace the ideal MHD with resistive MHD. This would reduce the stability boundary and lead to a lower prediction of the pedestal height. Figure 21 shows a schematic illustration of these proposed modifications.

11. Conclusions

This work has shown a clear empirical correlation between the pedestal pressure and the ratio $n_e^{\text{sep}}/n_e^{\text{ped}}$. Two different physics mechanisms can explain this correlation, as summarized in figure 22. In the range $0 < n_e^{\text{sep}}/n_e^{\text{ped}} < 0.4$, the increase of $n_e^{\text{sep}}/n_e^{\text{ped}}$ leads to the radial outwards shift of the position of the pressure profile, destabilizing PB modes and reducing the pedestal pressure. The effect saturates above $n_e^{\text{sep}}/n_e^{\text{ped}} \approx 0.4$, see figure 22(b). In the range $0.4 < n_e^{\text{sep}}/n_e^{\text{ped}} < 1.0$, the increase of $n_e^{\text{sep}}/n_e^{\text{ped}}$ reduces significantly $\nabla n_e/n_e$ and hence increases η_e . The increase of η_e leads to an increase in the slab-ETG turbulent transport (a change in $\nabla T_e/T_e$ can also affect the turbulent transport but this effect is not studied in this work), as can be seen by electron heat flux predicted with GENE, see figure 22(c). The increase of the turbulent transport strongly reduces the pedestal gradients and increases the level of auxiliary heating required to achieve a specified β_N . The reduction of the pedestal gradient reduces the temperature, increasing the resistivity in the pedestal region. Initial results with the CASTOR code suggests that resistive MHD might be necessary to explain the ELM triggering mechanism at $n_e^{\text{sep}}/n_e^{\text{ped}} > 0.4$.

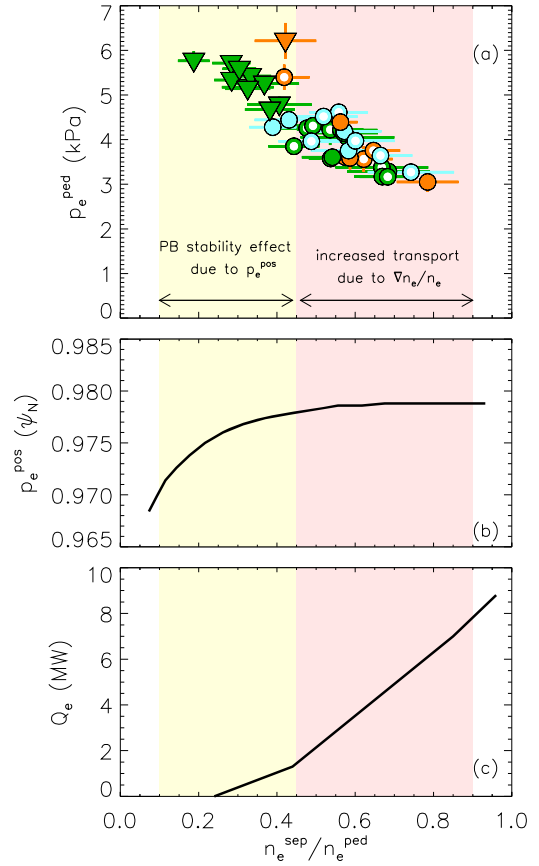


Figure 22. (a) Correlation between p_e^{ped} and $n_e^{\text{sep}}/n_e^{\text{ped}}$. (b) Behaviour of the p_e^{pos} vs $n_e^{\text{sep}}/n_e^{\text{ped}}$. (c) Behaviour of the turbulent heat flux predicted by GENE vs $n_e^{\text{sep}}/n_e^{\text{ped}}$.

Acknowledgments

This research is supported by Vetenskapsrådet, under Grant No. 2019-04618. This work has been carried out within the framework of the EUROfusion Consortium and has received funding from the Euratom Research and Training Programme 2014–2018 and 2019–2020 under Grant agreement No. 633053. The views and opinions expressed herein do not necessarily reflect those of the European Commission. This scientific paper has been published as part of the international project co-financed by the Polish Ministry of Science and Higher Education within the programme called ‘PMW’ for 2021.

Appendix

The work has assumed, systematically, $T_e^{\text{sep}} = 100$ eV. This assumption was motivated by the results from the two point model [33] and from EDGE2D-EIRENE simulations which showed that, in typical gas and power scans in JET-ILW, $T_e^{\text{sep}} = 100$ eV with a 20% variation at most [34]. Section 3.1 and earlier works [18, 24] have shown that this uncertainty does not affect significantly the temperature position and the PB stability analysis. Throughout the present work, the density position and the separatrix density have been determined

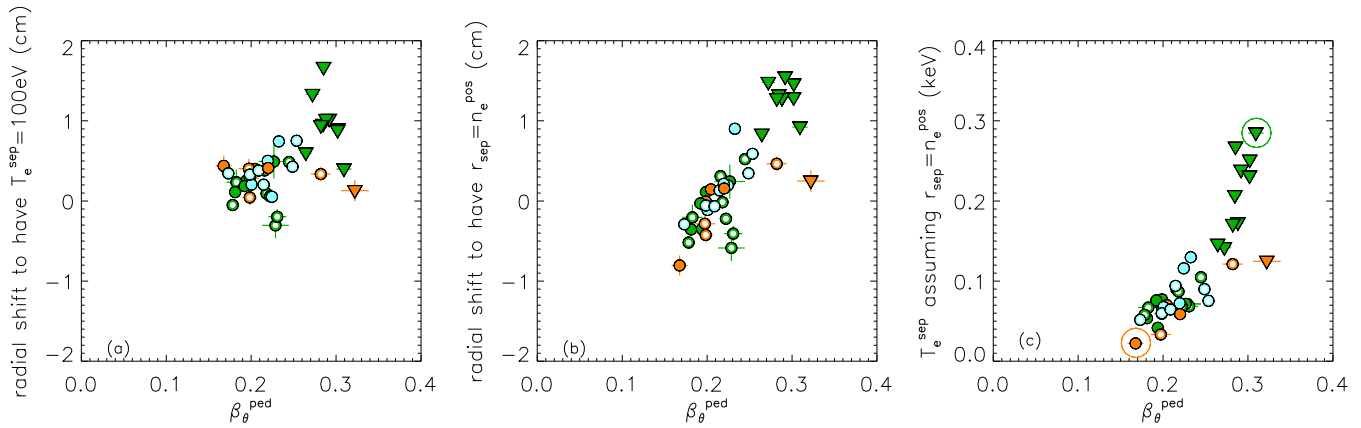


Figure 23. Radial shift in real space along the TS line of sight to have (a) $T_e^{\text{sep}} = 100$ eV and (b) $r^{\text{sep}} = n_e^{\text{pos}}$. (c) T_e^{sep} corresponding to the assumption $r^{\text{sep}} = n_e^{\text{pos}}$. The two circles in frame (c) highlight the two plasmas used in figure 24.

after the profiles were radially shifted to have $T_e^{\text{sep}} = 100$ eV. In this appendix, we show that a significantly less stringent assumption on T_e^{sep} cannot drastically alter our conclusions. In particular, we will show that (1) it is not reasonable to assume that n_e^{pos} is constant in our datasets and (2) that the disagreement between ideal MHD and experimental results cannot be resolved even assuming T_e^{sep} significantly different from 100 eV.

The radial shift in real space necessary to have $T_e = 100$ eV at the separatrix is shown in figure 23(a). The separatrix position has been determined in real space by calculating the intersection between the LCFS and the line of sight of TS diagnostic. The radial shift has been determined along the TS line of sight. The separatrix position has been determined with the best available equilibrium using the full set of available magnetic measurements which has been shown to improve the computed LCFS location [111]. EFIT++ reconstructions also including a pressure constraint were used for the JET-ILW dataset, while EFIT++ runs with only the improved magnetic constraints were adopted for the JET-C dataset (the pressure constrained cases for the JET-C dataset were not perfectly converged in the time interval of interest). For simplicity, figure 23(a) shows only the constant β_N datasets. The radial shift to have $T_e^{\text{sep}} = 100$ eV is in the range -0.3 cm/+1.5 cm, with most of the data that require a radial shift lower than 0.5 cm.

Figure 23(b) shows what the radial shift would be assuming constant n_e^{pos} , specifically, assuming $n_e^{\text{sep}} = r^{\text{sep}}$. This assumption requires a radial shift slightly larger than that of figure 23(a). This larger shift suggests that the $r^{\text{sep}} = n_e^{\text{pos}}$ assumption might be less reasonable than the usual $T_e^{\text{sep}} = 100$ eV assumption. This statement is significantly strengthened in figure 23(c), which shows the separatrix temperature corresponding to the assumption $r^{\text{sep}} = n_e^{\text{pos}}$. To have $r^{\text{sep}} = n_e^{\text{pos}}$, the separatrix temperature needs to vary from $T_e^{\text{sep}} \approx 20$ eV (for a high power/high gas rate JET-ILW pulse, see the orange circle) to $T_e^{\text{sep}} \approx 300$ eV (for a medium power/zero gas rate JET-C pulse, see the green circle). Given the EDGE2D-EIRENE results of gas and power scan discussed in reference

[34], a variation of T_e^{sep} in the range 20–300 eV is unreasonable. Moreover, using the two point model, $T_e^{\text{sep}} = 20$ eV and $T_e^{\text{sep}} = 300$ eV can be achieved in JET-ILW only with unrealistically low and high power, respectively $P_{\text{sep}} < 2$ MW and $P_{\text{sep}} \gg 30$ MW.

Nonetheless, we have assessed the impact of a very large variation of T_e^{sep} on the PB stability analysis. This has been done by determining critical pressure p_e^{crit} at which the PB modes become unstable, as described in section 3.2.1. The range tested is very large, from $T_e^{\text{sep}} = 20$ eV to $T_e^{\text{sep}} = 300$ eV. This range has been chosen to (i) have a direct link with the discussion of figure 23(c) and to (ii) prove beyond any reasonable doubt that the uncertainty on T_e^{sep} cannot explain the disagreement between the ELM triggering mechanism and the ideal PB stability. The test has been done for a JET-ILW and a JET-C plasma. For a direct link with the discussion on figure 23, these two pulses are those highlighted by circles in figure 23(c). The modelling results are shown in figure 24(a) with squared symbols. The experimental p_e^{ped} for the JET-C and the JET-ILW plasmas are shown with a triangle and a circle, respectively. At $T_e^{\text{sep}} = 100$ eV, the JET-C plasma is near the ideal PB boundary, as shown by the fact that the experimental p_e^{ped} is similar to the critical p_e^{ped} (the triangle and the green square overlap). Instead, at $T_e^{\text{sep}} = 100$ eV, the JET-ILW plasma is stable to ideal PB modes, as shown by the fact that the experimental p_e^{ped} is significantly lower than the critical p_e^{ped} . We can note that the increase of T_e^{sep} reduces the critical pressure (due to the outward shift of the profiles) but the critical p_e^{ped} overestimates the experimental p_e^{ped} even at $T_e^{\text{sep}} = 300$ eV. A further increase in T_e^{sep} would not reduce significantly the discrepancy as the effect starts to saturate. This saturation is due to the fact that the pedestal profiles are very steep, so a large variation in T_e^{sep} can lead only to a minor variation in T_e^{pos} , as shown in figure 24(b). For a link with figures 23(b) and (c), we can note that the assumption $r^{\text{sep}} = n_e^{\text{pos}}$ would lead to $T_e^{\text{sep}} = 20$ eV for this JET-ILW plasma. With $T_e^{\text{sep}} = 20$ eV the disagreement with ideal MHD would be even larger than at $T_e^{\text{sep}} = 100$ eV. For the JET-C plasma, figure 23(c) would suggest $T_e^{\text{sep}} = 300$ eV. At $T_e^{\text{sep}} = 300$ eV the good agreement between experimental JET-C pedestal and

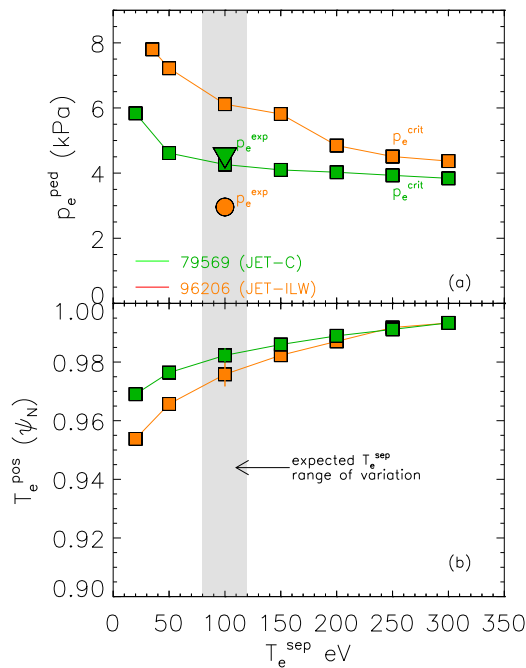


Figure 24. (a) Pedestal pressure versus T_e^{sep} . The circle and the triangle highlight the experimental pressure of a JET-ILW and JET-C plasma, respectively. The squares highlight the corresponding critical pressure determined with ideal MHD. (b) Corresponding position of the pedestal temperature versus the assumed T_e^{sep} .

the ideal PB modelling is lost. This further suggests that the assumption $r^{\text{sep}} = n_e^{\text{pos}}$ is not the most reasonable.

The conclusion is that, at present, the assumption $T_e^{\text{sep}} = 100$ eV is still the most reasonable. Different assumptions would lead unreasonably high or low T_e^{sep} and would increase the disagreement between experimental data and ideal MHD stability. Furthermore, any uncertainty on the $T_e^{\text{sep}} = 100$ eV assumption cannot reconcile the ELM triggering mechanism with ideal MHD stability.

ORCID iDs

L. Frassinetti <https://orcid.org/0000-0002-9546-4494>
 C. Perez von Thun <https://orcid.org/0000-0002-1166-2179>
 B. Chapman <https://orcid.org/0000-0001-9879-2285>
 L. Horvath <https://orcid.org/0000-0002-5692-6772>
 R. Bianchetti Morales <https://orcid.org/0000-0003-0667-3356>
 M. Dunne <https://orcid.org/0000-0002-5259-9970>
 A.R. Field <https://orcid.org/0000-0003-0671-9668>
 D. Hatch <https://orcid.org/0000-0002-1625-4385>
 C.F. Maggi <https://orcid.org/0000-0001-7208-2613>
 C.M. Roach <https://orcid.org/0000-0001-5856-0287>
 E.R. Solano <https://orcid.org/0000-0002-4815-3407>

References

- [1] Brezinszek S. et al 2012 Fuel retention studies with the ITER-like wall in JET 2012 IAEA Fusion Energy Conf.

- (San Diego) (http://www-naweb.iaea.org/napc/physics/FEC/FEC2012/papers/488_EX41.pdf) EX/4-1
- [2] Matthews G.F. et al 2013 J. Nucl. Mater. **438** S2
- [3] Beurskens M. et al 2014 Nucl. Fusion **54** 043001
- [4] Garzotti L. et al 2019 Nucl. Fusion **59** 076037
- [5] Mailloux J. et al Overview of JET results for optimising ITER operation Nucl. Fusion (submitted).
- [6] Giroud C. et al 2013 Nucl. Fusion **53** 113025
- [7] Giroud C. et al 2015 Plasma Phys. Control. Fusion **57** 035004
- [8] Giroud C. et al 2018 Optimisation of JET-DT and ITER operation by developing an understanding of the role of low-Z impurity on the H-mode pedestal 2018 IAEA Fusion Energy Conf. (Gandhinagar) (<https://nucleus.iaea.org/sites/fusionportal/Shared%20Documents/FEC%202018/fec2018-preprints/preprint0347.pdf>) EX/3-3.
- [9] Reinke M.L., Hughes J.W., Loarte A., Brunner D., Hutchinson I.H., LaBombard B., Payne J. and Terry J.L. 2011 J. Nucl. Mater. **415** S340
- [10] Beurskens M. et al 2013 Plasma Phys. Control. Fusion **55** 124043
- [11] Dunne M.G. et al 2017 Plasma Phys. Control. Fusion **59** 025010
- [12] Beurskens M.N.A. et al 2016 Nucl. Fusion **56** 056014
- [13] Dunne M. 2018 Impact of impurity seeding on pedestal structure in ASDEX Upgrade and Alcator C-Mod IAEA Fusion Energy Conf. (Gandhinagar, India) (<https://nucleus.iaea.org/sites/fusionportal/Shared%20Documents/FEC%202018/fec2018-preprints/preprint0585.pdf>) EX/P8-2.
- [14] Nunes I. 2016 Plasma Phys. Control. Fusion **58** 014034
- [15] Maggi C.F. et al 2015 Nucl. Fusion **55** 113031
- [16] Schneider P.A., Orte L.B., Burckhart A., Dunne M.G., Fuchs C., Gude A., Kurzan B., Suttrop W. and Wolfrum E. (The ASDEX Upgrade Team) 2015 Plasma Phys. Control. Fusion **57** 014029
- [17] Stefanikova E. et al 2018 Nucl. Fusion **58** 056010
- [18] Frassinetti L. et al 2019 Nucl. Fusion **59** 076038
- [19] Stefanikova E., Frassinetti L., Saarelma S., Perez von Thun C. and Hillesheim J.C. (JET Contributors) 2021 Nucl. Fusion **61** 026008
- [20] Dunne M.G. et al 2017 Plasma Phys. Control. Fusion **59** 014017
- [21] Wang H.Q. et al 2018 Nucl. Fusion **58** 096014
- [22] Moser A.L., Casali L., Covele B.M., Leonard A.W., McLean A.G., Shafer M.W., Wang H.Q. and Watkins J.G. 2020 Phys. Plasmas **27** 032506
- [23] Casali L., Eldon D., Boedo J.A., Leonard T. and Covele B. 2020 Nucl. Fusion **60** 076011
- [24] Frassinetti L. et al 2021 Nucl. Fusion **61** 016001
- [25] Diallo A., Groebner R.J., Rhodes T.L., Battaglia D.J., Smith D.R., Osborne T.H., Canik J.M., Guttenfelder W. and Snyder P.B. 2015 Phys. Plasmas **22** 056111
- [26] Diallo A., Dominski J., Barada K., Knolker M., Kramer G.J. and McKee G. 2018 Phys. Rev. Lett. **121** 235001
- [27] Maggi C.F. et al 2017 Nucl. Fusion **57** 116012
- [28] Saarelma S., Challis C.D., Garzotti L., Frassinetti L., Maggi C.F., Romanelli M. and Stokes C. 2018 Plasma Phys. Control. Fusion **60** 014042
- [29] Zohm H. et al 1996 Plasma Phys. Control. Fusion **38** 105
- [30] Pasqualotto R., Nielsen P., Gowers C., Beurskens M., Kempenaars M., Carlstrom T. and Johnson D. 2004 Rev. Sci. Instrum. **75** 3891
- [31] Groebner R.J. et al 2001 Nucl. Fusion **41** 1789
- [32] Frassinetti L., Beurskens M.N.A., Scannell R., Osborne T.H., Flanagan J., Kempenaars M., Maslov M., Pasqualotto R. and Walsh M. 2012 Rev. Sci. Instrum. **83** 013506
- [33] Kallenbach A., Asakura N., Kirk A., Korotkov A., Mahdavi M.A., Mossessian D. and Porter G.D. 2005 J. Nucl. Mater. **337–339** 381–5

- [34] Simpson J., Moulton D., Giroud C., Groth M. and Corrigan G. 2019 *Nucl. Mater. Energy* **20** 100599
- [35] Saarelma S. et al 2015 *Phys. Plasmas* **22** 056115
- [36] Huysmans G.T.A. et al 1991 *Computational Physics: Proc. Int. Conf.* (Amsterdam, The Netherlands) (Singapore: World Scientific)
- [37] Sauter O., Angioni C. and Lin-Liu Y.R. 1999 *Phys. Plasmas* **6** 2834
- [38] Wilson H.R., Snyder P.B., Huysmans G.T.A. and Miller R.L. 2002 *Phys. Plasmas* **9** 1277
- [39] Miller R.L., Chu M.S., Greene J.M., Lin-Liu Y.R. and Waltz R.E. 1998 *Phys. Plasmas* **5** 973
- [40] Saarelma S., Alfier A., Beurskens M.N.A., Coelho R., Koslowski H. R., Liang Y. and Nunes I. 2009 *Plasma Phys. Control. Fusion* **51** 035001
- [41] Aiba N. et al 2017 *Nucl. Fusion* **57** 126001
- [42] Aiba N. et al 2018 *Plasma Phys. Control. Fusion* **60** 014032
- [43] Frassinetti L. et al 2017 *Nucl. Fusion* **57** 016012
- [44] Kerner W. 1998 *J. Comput. Phys.* **142** 271–303
- [45] Saarelma S., Frassinetti L., Bilkova P., Challis C.D., Chankin A., Fridström R., Garzotti L., Horvath L. and Maggi C.F. 2019 *Phys. Plasmas* **26** 072501
- [46] Snyder P.B., Groebner R.J., Leonard A.W., Osborne T.H. and Wilson H.R. 2009 *Phys. Plasmas* **16** 056118
- [47] Snyder P.B., Groebner R.J., Hughes J.W., Osborne T.H., Beurskens M., Leonard A.W., Wilson H.R. and Xu X.Q. 2011 *Nucl. Fusion* **51** 103016
- [48] Romanelli M. et al 2014 *Plasma Fusion Res.* **9** 3403023
- [49] Reiter D. et al 1992 *J. Nucl. Mater.* **196** 80–89
- [50] Simonini R., Corrigan G., Radford G., Spence J. and Taroni A. 1994 *Contrib. Plasma Phys.* **34** 368
- [51] Wiesen S. 2006 *EDGE2D/EIRENE Code Interface Report* Institut für Energie- und Klimaforschung / Plasma-physik (IEK-4) Forschungszentrum Jülich GmbH D-52425 Jülich, Germany IRCReport (http://eirene.de/e2deir_report_30jun06.pdf)
- [52] Cenacchi G. and Taroni A. 1988 *Rapporto ENEA RT/TIB(88)5 19097143*
- [53] Jenko F., Dorland W., Kotschenreuther M. and Rogers B.N. 2000 *Phys. Plasmas* **7** 1904
- [54] Görler T. et al 2016 *Phys. Plasmas* **23** 07053
- [55] Hughes J.W. et al 2011 *Nucl. Fusion* **51** 083007
- [56] de la Luna E. et al 2016 Recent results on high-triangularity H-mode studies in JET-ILW 2016 *IAEA Fusion Energy Conf.* (Kyoto) (<https://nucleus.iaea.org/sites/fusionportal/Shared%20Documents/FEC%202016/fec2016-preprints/preprint0345.pdf>) EX/P6-11
- [57] Reimold F., Wischmeier M., Potzel S., Guimarães L., Reiter D., Bernert M., Dunne M. and Lunt T. 2017 *Nucl. Mater. Energy* **12** 193
- [58] Groth M. et al 2013 *Nucl. Fusion* **53** 093016
- [59] Groth M. et al 2015 *J. Nucl. Mater.* **463** 471
- [60] Uljanovs J. et al 2017 *Nucl. Mater. Energy* **12** 791–7
- [61] Lomanowski B. et al 2020 The role of the target electron temperature as a key detachment parameter in different JET-ILW divertor configurations 62nd Annual Meeting of the APS Division of Plasma Physics WI02.00001 (9–13 November 2020) (https://absimage.aps.org/image/DPP20/MWS_DPP20-2020-000938.pdf)
- [62] Lomanowski B. 2021 (private communication)
- [63] Potzel S. et al 2015 *J. Nucl. Mater.* **463** 541
- [64] Hughes J.W., LaBombard B., Mossessian D.A., Hubbard A.E., Terry J. and Biewer T. (The Alcator C-Mod Team) 2006 *Phys. Plasmas* **13** 056103
- [65] Mordijck S. et al 2020 *Nucl. Fusion* **60** 082006
- [66] Hatch D.R., Kotschenreuther M., Mahajan S., Valanju P. and Liu X. 2017 *Nucl. Fusion* **57** 036020
- [67] Jenko F., Told D., Xanthopoulos P., Merz F. and Horton L.D. 2009 *Phys. Plasmas* **16** 055901
- [68] Tamain P., Bufferand H., Ciraolo G., Colin C., Galassi D., Ghendrih P., Schwander F. and Serre E. 2016 *J. Comput. Phys.* **321** 606
- [69] Sheikh U.A. et al 2019 *Plasma Phys. Control. Fusion* **61** 014002
- [70] Beurskens M.N.A. et al (The DIII-D Team, The ASDEX Upgrade Team, and JET-EFDA Contributors) 2011 *Phys. Plasmas* **18** 056120
- [71] Osborne T.H. et al 2015 *Nucl. Fusion* **55** 063018
- [72] Hughes J.W., LaBombard B., Terry J., Hubbard A. and Lipschultz B. 2007 *Nucl. Fusion* **47** 1057
- [73] Maingi R. et al (NSTX Research Team) 2009 *Phys. Rev. Lett.* **103** 075001
- [74] Maingi R. et al 2012 *Nucl. Fusion* **52** 083001
- [75] Hatch D.R. et al 2019 *Nucl. Fusion* **59** 086056
- [76] Yan Z. et al 2011 *Phys. Rev. Lett.* **107** 055004
- [77] Diallo A. et al 2013 *Phys. Plasmas* **20** 012505
- [78] Diallo A. et al 2014 *Phys. Rev. Lett.* **112** 115001
- [79] Dickinson D. et al 2012 *Phys. Rev. Lett.* **108** 135002
- [80] Kotschenreuther M. et al 2019 *Nucl. Fusion* **59** 096001
- [81] Diallo A. and Laggner F.M. 2021 *Plasma Phys. Control. Fusion* **63** 013001
- [82] Hatch D. et al 2019 *Nucl. Fusion* **61** 036015
- [83] Guttenfelder W., Groebner R.J., Canik J.M., Grierson B.A., Belli E.A. and Candy J. 2021 *Nucl. Fusion* **61** 056005
- [84] Barada K. et al New understanding of multi-scale/multi-field pedestal turbulence, transport, and gradient behavior during type-I ELMs on the DIII-D tokamak *Nucl. Fusion* (submitted)
- [85] Chapman B. 2021 (private communication)
- [86] Field A.R. et al 2020 *Plasma Phys. Control. Fusion* **62** 055010
- [87] Parisi J.F. et al 2020 *Nucl. Fusion* **60** 126045
- [88] Belli E.A. and Candy J. 2012 *Plasma Phys. Control. Fusion* **54** 015015
- [89] Leyland M.J. et al 2015 *Nucl. Fusion* **55** 013019
- [90] Walk J.R., Snyder P.B., Hughes J.W., Terry J.L., Hubbard A.E. and Phillips P.E. 2012 *Nucl. Fusion* **52** 063011
- [91] Schneider P.A. et al 2012 *Plasma Phys. Control. Fusion* **54** 105009
- [92] Groebner R. et al 2013 *Nucl. Fusion* **53** 093024
- [93] Urano H., Takizuka T., Kamada Y., Oyama N. and Takenaga H. 2008 *Nucl. Fusion* **48** 045008
- [94] Urano H. et al 2009 *Nucl. Fusion* **49** 095006
- [95] Urano H., Aiba N., Kamiya K. and Kamada Y. 2016 *Nucl. Fusion* **56** 016005
- [96] Pamela S.J.P. et al 2017 *Nucl. Fusion* **57** 076006
- [97] Field A.R. 2021 (private communication)
- [98] Hatch D.R., Kotschenreuther M., Mahajan S., Valanju P., Jenko F., Told D., Görler T. and Saarelma S. 2016 *Nucl. Fusion* **56** 104003
- [99] Pamela S. et al 2016 *Plasma Phys. Control. Fusion* **58** 014026
- [100] Pamela S.J.P., Huysmans G.T.A., Beurskens M.N.A., Devaux S., Eich T. and Benkadda S. 2011 *Plasma Phys. Control. Fusion* **53** 054014
- [101] Garcia J. et al 2021 Integrated scenario development at JET for DT operation and ITER risk mitigation 2020 *IAEA Fusion Energy Conf.* (Nice) (<https://nucleus.iaea.org/sites/fusionportal/Shared%20Documents/FEC%202020/fec2020-preprints/preprint0989.pdf>) EX/1-2
- [102] de la Luna E. et al 2021 Exploring the physics of a high-performance H-mode with small ELMs and zero gas dosing in JET-ILW 2020 *IAEA Fusion Energy Conf.* (Nice) (<https://nucleus.iaea.org/sites/fusionportal/Shared%20Documents/FEC%202020/fec2020-preprints/preprint1094.pdf>) EX/3-2

- [103] Schweinzer J. *et al* 2011 *Nucl. Fusion* **51** 113003
- [104] Challis C.D. *et al* 2015 *Nucl. Fusion* **55** 053031
- [105] Sheikh U.A. *et al* 2021 *Nucl. Mater. Energy* **26** 100933
- [106] Snyder P.B. *et al* 2019 *Nucl. Fusion* **59** 086017
- [107] Kukushkin A.S., Pacher H.D., Kotov V., Reiter D., Coster D. and Pacher G.W. 2007 *Nucl. Fusion* **47** 698
- [108] Romanelli M. *et al* 2015 *Nucl. Fusion* **55** 093008
- [109] Garzotti L. *et al* 2019 *Nucl. Fusion* **59** 026006
- [110] Snyder P. *et al* 2019 Impact of fueling and separatrix density on the pedestal in peeling and ballooning limited regimes *17th Int. Workshop on H-mode Physics and Transport Barriers* (Shanghai, China, 9–11 October 2019)
- [111] Szepesi G. *et al* 2021 Advanced equilibrium reconstruction for JET with EFIT++ *47th EPS Conf. Plasma Physics* (21–25 June 2021) p P3.1037 (<http://ocs.ciemat.es/EPS2021PAP/pdf/P3.1037.pdf>)